Open Access Earth System Science Data Discussions

1 C-band radar data and in situ measurements for the monitoring of
2 wheat crops in a semi-arid area (center of Morocco)

3 Nadia Ouaadi[1,2], Jamal Ezzahar[3,4], Saïd Khabba[1,4], Salah Er-Raki[4,5], Adnane Chakir[1], Bouchra Ait
4 Hssaine[4], Valérie Le Dantec[3], Zoubair Rafi[1,2], Antoine Beaumont[6], Mohamed Kasbani[3], Lionel Jarlan[3]

5 [1]LMFE, Department of Physics, Faculty of Sciences Semlalia, Cadi Ayyad University, Marrakech, Morocco
6 [2]CESBIO, University of Toulouse, IRD/CNRS/UPS/CNES, Toulouse, France
7 [3]MISCOM, National School of Applied Sciences, Cadi Ayyad University, Safi, Morocco.
8 [4]CRSA, Mohammed VI Polytechnic University UM6P, Benguerir, Morocco.
9 [5]ProcEDE, Department of Applied Physics, Faculty of Sciences and Technologies, Cadi Ayyad University, Marrakech,
10 Morocco.
11 [6]Atmo Hauts-de-France, Lille, France.

12 *Correspondence to*: J. Ezzahar (j.ezzahar@uca.ma)

13 **Abstract.** A better understanding of the hydrological functioning of irrigated crops using remote sensing observations is of
14 prime importance in the semi-arid areas where the water resources are limited. Radar observations, available at high
15 resolution and revisit time since the launch of Sentinel-1 in 2014, have shown great potential for the monitoring of the water
16 content of the upper soil and of the canopy. In this paper, a complete set of data for radar signal analysis is shared to the
17 scientific community for the first time to our knowledge. The data set is composed of Sentinel-1 products and in situ
18 measurements of soil and vegetation variables collected during three agricultural seasons over drip-irrigated winter wheat in
19 the Haouz plain in Morocco. The in situ data gathers soil measurements (time series of half-hourly surface soil moisture,
20 surface roughness and agricultural practices) and vegetation measurements collected every week/two weeks including above-
21 ground fresh and dry biomasses, vegetation water content based on destructive measurements, cover fraction, leaf area index
22 and plant height. Radar data are the backscattering coefficient and the interferometric coherence derived from Sentinel-1
23 GRDH (Ground Range Detected High resolution) and SLC (Single Look Complex) products, respectively. The normalized
24 difference vegetation index derived from Sentinel-2 data based on Level-2A (surface reflectance and cloud mask)
25 atmospheric effects-corrected products is also provided. This database, which is the first of its kind made available in open
26 access, is described here comprehensively in order to help the scientific community to evaluate and to develop new or
27 existing remote sensing algorithms for monitoring wheat canopy under semi-arid conditions. The data set is particularly
28 relevant for the development of radar applications including surface soil moisture and vegetation parameters retrieval using
29 either physically based or empirical approaches such as machine and deep learning algorithms.
30 The database is archived in the DataSuds repository and is freely-accessible via the DOI: https://doi.org/10.23708/8D6WQC
31 (Ouaadi et al., 2020a).

1 Introduction

The south-Mediterranean region has been identified as a hot spot of climate change (Giorgi, 2006; Giorgi and Lionello, 2008; IPCC, 2014) that may worsen the water shortage already affecting the region. Up to 90% of available water is dedicated to irrigation (Ministre de l'agriculture et peche maritime du develpement rurale et des eaux et forets, 2018). Indeed, the predicted temperature rise that could reach 3°C by 2050 combined to precipitation decrease and increased evapotranspiration could drastically increase the irrigation requirements. The demand for water is also already increasing in response to an ever-growing population and to changes of agricultural practices-intensification, conversion to cash crops, rise of irrigated areas (Ducrot et al., 2004; Fader et al., 2016; Jarlan et al., 2016). The monitoring of irrigated crops and the optimization of water use is therefore of prime importance for the sustainability of the water resources in the Mediterranean region. This requires the implementation of methods to monitor the crop water status and the underlying soil moisture (Wang et al., 2012).

Within this context, the observations from active spaceborne sensors in the microwave domain (radar) have shown great potential for the monitoring of crops (Mattia et al., 2003; Ouaadi et al., 2020b; Picard et al., 2003). The potential of radar data for monitoring irrigated crops originates from their high sensitivity to the water status of the surface including the water content of the above ground biomass and the moisture of the upper soil layer (Ulaby and Dobson, 1986). It is also sensitive to the structural properties of the observed target including the size and orientation of the canopy elements (leaves, steams, trunks) and the soil roughness. A key advantage of radar observations for monitoring crops, especially those crops growing during the rainy season such as wheat, is also that it is not prone to atmospheric perturbations. Sentinel-1 provides for the first time since 2014 backscattering coefficients at a resolution of 10 m and a revisit time of 6 days compatible with the high dynamic of annual crops at the field scale paving the way to an operational use of C-band radar data for crop monitoring.

Nevertheless, radar signal is a complex mix of backscattering from the soil and from the canopy that are often difficult to disentangle. The impact of any changes of the canopy structure such as the appearance of the heads during the heading stage of wheat (Brown et al., 2003; El Hajj et al., 2019; Ulaby et al., 1986) or of the soil roughness may also drastically impact the backscattering response. These processes are not fully understood and not always properly reproduced by the backscattering models.

The sensitivity of the backscattering coefficient to the surface soil moisture (SSM) is widely documented in the literature for bare or covered soils (Ezzahar et al., 2020; Ouaadi et al., 2020c, 2020b; Ulaby and Dobson, 1986; Zribi et al., 2014). Several retrieval approaches based on the inversion of a radiative transfer models (Bai et al., 2017; Gherboudj et al., 2011; El Hajj et al., 2016; Li and Wang, 2018; Ouaadi et al., 2020b) or based on linear or non-linear empirical regression (Gorrab et al., 2015; Ouaadi et al., 2020b) have been developed. The SSM derived from radar observations are also used to estimate RZSM (root zone soil moisture), a key variable in agronomy, through the combination with a land surface model (Cho et al., 2015; Das et al., 2008; Dumedah et al., 2015; Ford et al., 2014; Rodell et al., 2004; Sabater et al., 2006; Sure and Dikshit, 2019).

64 The presence of a canopy above the soil results in two more contributions to the backscattered signal: the volume scattering

65 and the attenuated signal by the canopy. The water content of vegetation influences the dielectric properties, that in turn

66 influence the radar backscatter from the vegetation (Ulaby et al., 1982). Based on these findings, some studies are focused on

67 the retrieval of vegetation parameters from SAR (Synthetic Aperture Radar) data such as above-ground biomass (Hosseini

68 and McNairn, 2017; Periasamy, 2018; Taconet et al., 1994) or even grain yield (Fieuzal et al., 2013; Patel et al., 2006). In

69 addition to the backscattering coefficient, the polarization ratio and the interferometric coherence have demonstrated

70 potentialities for the characterization of the vegetation including height (Blaes and Defourny, 2003; Engdahl et al., 2001),

71 vegetation cover fraction (Wegmuller and Werner, 1997), fresh above-ground biomass (Mattia et al., 2003; Veloso et al.,

72 2017), above-ground biomass (Ouaadi et al., 2020b) and vegetation water content (Ouaadi et al., 2020b). Other studies

73 acknowledge the sensitivity of coherence to soil moisture (De Zan et al., 2014; Scott et al., 2017). Recent research suggests

74 that radar observations could also provide valuable information on the canopy water status (Van Emmerik et al., 2015;

75 Ouaadi et al., 2020d) for crop stress detection.

76 In situ measurements of vegetation and soil characteristics are always needed to improve our understanding of the radar

77 response, to develop and calibrate radiative transfer models and to propose generic retrieval methods for the inversion of soil

78 or vegetation variables. Nevertheless, in situ data set dedicated to these objectives are really specific in the sense that, for

79 instance, soil roughness is only of interest for understanding the physical principle of observations in the microwave domain.

80 Likewise, above-ground biomass is often measured by agronomist for crop modeling for instance but the partition between

81 dry and wet matter, a key variable for radar acquisition, is hardly ever done. Indeed, the latter relies on heavy destructive

82 measurements consisting in cutting all the vegetation elements within squares sample in the field and a double weighting

83 before and after drying the samples in an oven. In this paper, a recent, multi-year and complete database composed of

84 processed Sentinel-1 SAR data (the backscattering coefficient and the interferometric coherence), Sentinel-2 NDVI and

85 measured variables on the soil, on the vegetation and on the agricultural practices are made available. The in situ data

86 include automatic measurements as well as observations carried out during measurement campaigns once or twice every 15

87 days throughout the growing season. This database covers 3 wheat seasons (2016-2017 to 2018-2019) of 3 different irrigated

88 fields (Ouaadi et al., 2020b). It is a unique and valuable data set that can be used for vegetation and soil moisture monitoring

89 applications including from radar observations. In addition, the multiyear database can be useful for multiyear time series

90 analysis. In the next section, an overview of the field-location and a detailed description of the variables, including field

91 measurements and remote sensing data processing, are presented. In Section 3, the variables are experimentally and

92 physically analyzed to assess the consistency of the dataset. Conclusions are provided in Section 4.

2   Study area and experimental sites

2.1 Study area

The database described in this paper is collected in the Haouz plain in the Tensift watershed, center of Morocco (Fig. 1). This plain is one of the most important plains in Morocco located at 550 m above sea level and covers about 6000 km^2 of which 2000 km^2 are irrigated. The climate in the region is Mediterranean semi-arid, with an annual average precipitation of about 250 mm. The distribution of precipitations highlights a wet season with around 85% of annual precipitations between October and April, and a dry season from May to September. The maximum average of temperature occurs during summer in July-August (about 35°C) and the minimum in January (about 5°C) (Abourida et al., 2008). The average air humidity is about 50% and the reference evapotranspiration ET0 is around 1600 mm/year (Jarlan et al., 2015), which is greatly exceeding the annual rainfall. The agricultural production in the plain is not very diverse, focusing on cereals (51% of the irrigated areas), olive trees (30% of the irrigated area), 9% of fodder production and 2% of market gardening for cattle breeding while the non-irrigated part of the plain is cropped with rainfed wheat (Abourida et al., 2008). Wheat is usually sown between November and January depending on precipitation distribution, even for irrigated field, and on cultivar. Harvest usually occurs in May or June.

2.2 Experimental sites

The database concerns three irrigated fields (F1, F2 and F3) located within a private farm in the province of Chichaoua located 65 Km west of Marrakech city (Fig. 1). F1 and F2 are monitored during two successive growing seasons (2016-2017 and 2017-2018) while F3 is monitored during the season 2018-2019. The fields are sown using an automatic seed drill. They are irrigated using the drip technique. For all the fields, the wheat is cropped once a year during winter-spring (see Table 1 for sowing and harvest dates). After harvest, the fields are generally used for cattle grazing until mid-July when the plowing works started. Table 1 summarizes some general information about the fields. Please note that during the 2017-2018 season, wheat in F2 is affected by specific growing conditions: i) the development of adventices belonging to the wild thistles family characterized by a horizontal structure, ii) the seeding density is higher than in F1, and iii) the seeding is a mixture of barley and wheat within F2. This resulted in very long stems: 146 cm in F2 compared to 110 cm in F1 in April 2018. Finally, these long stems in F2 are laid down by the wind from April 12, 2018. A picture of F2 during 2017-2018 is provided in appendix A (Fig. A1). Although such exceptional growing conditions are not very likely, it has been chosen to include this crop season in the data set to cover different conditions of growth.

120
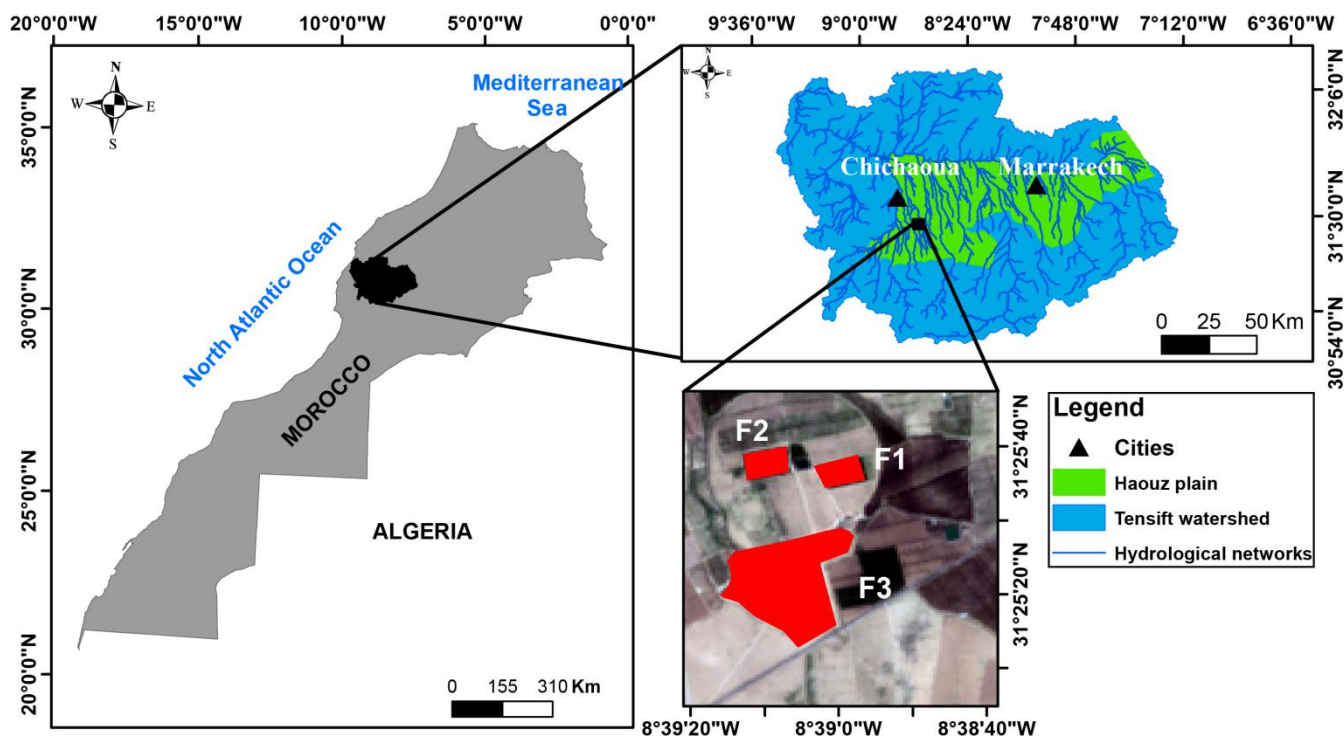
121
122 **Figure 1. Location of the study fields: F1, F2 and F3 are drip-irrigated wheat plots in a private farm ("Domaine Rafi") near**
123 **Chichaoua city in the Haouz plain, center of Morocco.**

124 **Table 1. General information about the three fields**

| Field	Area (ha)	Season	Sowing date	Harvest date	Irrigation	Sand (%)	Clay(%)
F1	1.5	2016-2017 & 2017-2018	Nov 25, 2016	May 16, 2017	Drip technique	32.5	37.5
F2	1.5		Nov 27, 2017	June 08, 2018			
F3	12	2018-2019	Nov 04, 2018	June 06, 2019			

125 **3 Database**

126 **3.1 Field datasets**

127 **3.1.1 Soil moisture**

128 SSM is automatically measured every 30 min using Time Domain Reflectometry sensors (TDR), (Campbell Scientific
129 CS616) using two sensors buried at a depth of 5 cm: one under the drippers and another one between. The average is

5

130   computed in order to get a representative SSM value of the field. In addition, similar sensors are buried for RZSM measuring

131   at 25 and 35 cm of depth over F1 and F3 while one sensor is buried at 30 cm over F2. Figure 2a illustrates an example of

132   TDR sensors at different depths.
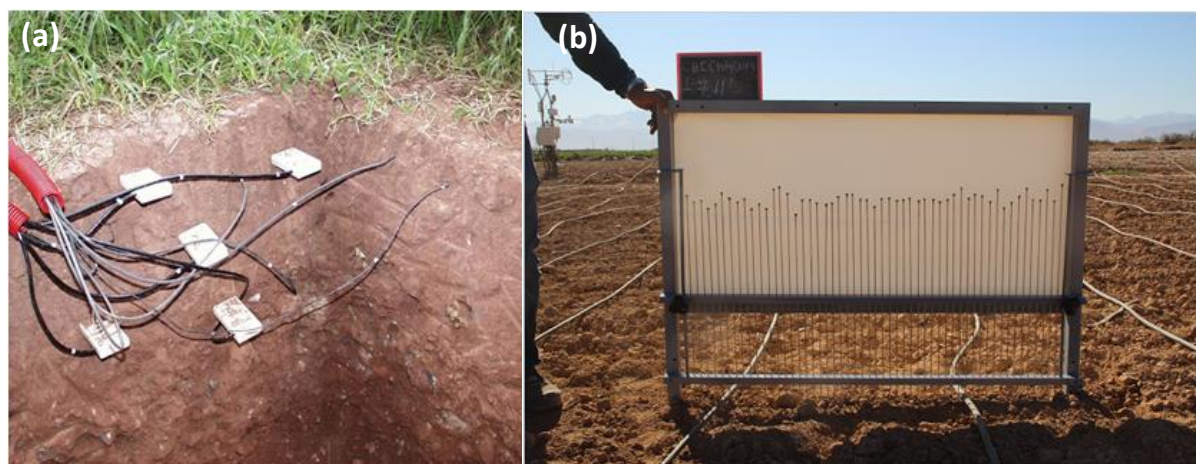
134   **Figure 2. Examples of (a) TDR sensors installed at different depths and b) a pin profiler picture taken over one of the ploughed**
135   **field with drip irrigation tubes installed.**

136   TDR sensors are calibrated using the gravimetric technique. The calibration is done during 2016-2017 season using samples

137   taken from the first 5 cm from both fields F1 and F2 and then the calibrated equation is applied to F1, F2 and F3 data as the

138   soil characteristics are similar and the same sensors are used. For that purpose, an aluminum core of 392.5 cm^3 is used to

139   collect samples at the TDR installation depths. Three samples are collected per day and per field during five days chosen

140   with different soil moisture conditions in order to cover a wide range of values (0.08 to 0.33 m^3/m^3). A linear regression is

141   established between the volumetric water content and the square root of the TDR time response (named τ in second) as

142   follow:

$$SSM = a_{TDR} * \sqrt{\tau} + b_{TDR} \tag{1}$$

144   The calibrated values using data of both fields are $a_{TDR} = 0.275 \, m^3/m^3/s^{0.5}$ and $b_{TDR} = -1.154 \, m^3/m^3$. Figure 3

145   illustrates the calibration results with all the samples displayed. The statistical metrics are: correlation coefficient R = 0.97,

146   Root Mean Square Error RMSE = 0,018 m^3/m^3 and no Bias. When considering both fields separately, the results for (F1, F2)

147   are R = (0.90, 0.94), RMSE = (0.023, 0.01) m^3/m^3 and Bias = (-0.002, 0.003) m^3/m^3.

148   The calibrated equation is also applied for the RZSMs assuming that the soil properties are the same at different depths.

149   Figure A2 in appendix A illustrates an example of an RZSM time series over F1.

Open Access Earth System Science Data Discussions
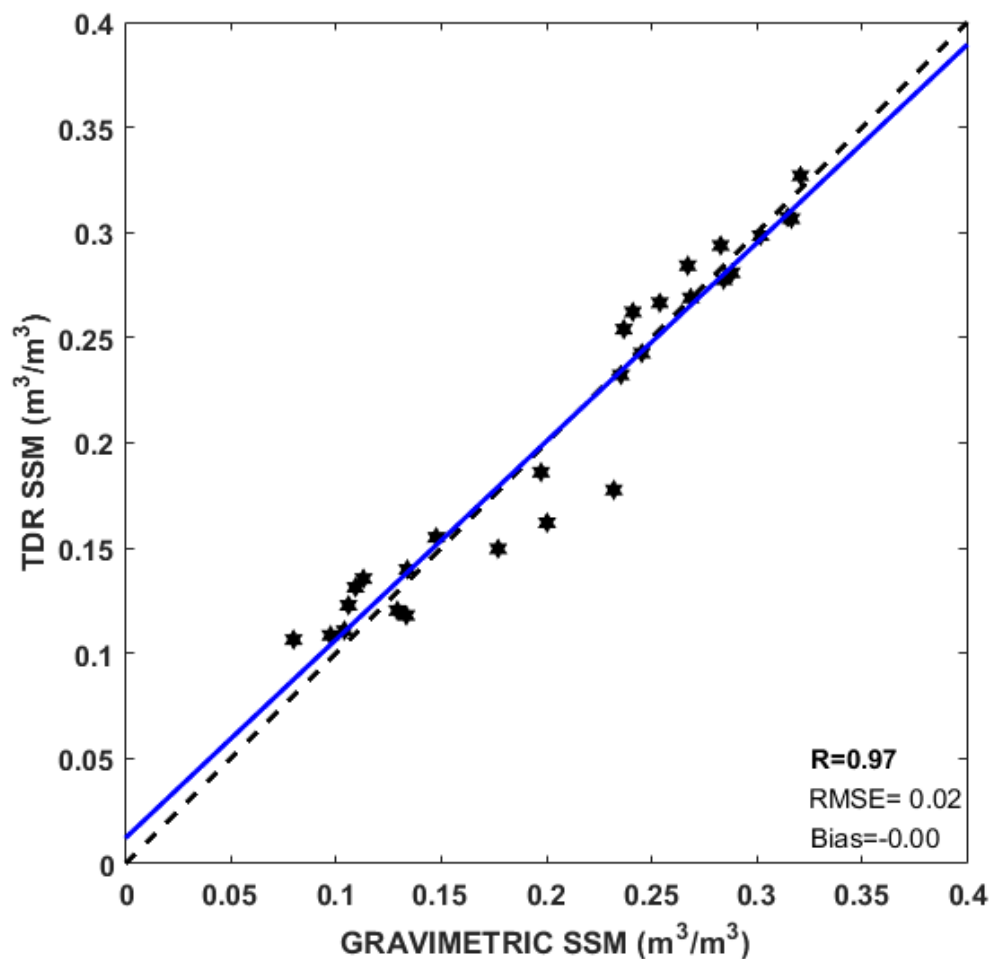
Figure 3. Surface soil moisture measured by TDR versus gravimetric measurements using samples collected over both fields F1 and F2 during 2016-2017 growing season. The blue solid line is the linear regression and the dashed line is Y=X.

3.1.2 Surface roughness

Surface roughness characterizes the micro variation of the ground surface elevation within a given area/field (Allmaras et al., 1966). It is a parameter that affect particularly the SAR signal and to a lesser extent the visible and near infrared (Girard and Girard, 1989). The two parameters that characterize the surface roughness are the root mean square height (h_{rms}) and the correlation length (L). h_{rms} provides a vertical descriptor of ground roughness by measuring the elevation of the surface along one or more observation lines and calculating the standard deviation of the recorded values. The second parameter (L) corresponds to the distance between measurements from which the heights between points are statistically independent. This parameter provides a horizontal description of the ground surface roughness, more specifically the organizational structure and spatial continuity of the microtopography (Nolin et al., 2005). Over the 3 studied fields, measurements of the surface

162 roughness are taken during the first stage of wheat when the ground is not totally covered by the canopy. We used a pin

163 profiler of 1 m length, composed of a set of 53 metal needles of equal length every 2 cm (Fig. 2b). 16 sample pictures are

164 taken per field and per date including eight pictures parallel and eight pictures perpendicular to the rows direction. The

165 pictures are taken using Canon 6EOS 600D equipped with TAMRON lens (Model A14).

166 The images are processed in MATLAB based on the detection of the top position of each needle. h_{rms} and L are computed

167 from the correlation function and then the average per direction, per field and per date is computed. For illustration, Fig. 4

168 shows the time series of h_{rms} and L parameters computed separately for each direction for F1 and F2 during the season 2017-

169 2018 while the average value per season are summarized in Table 2 for F1, F2 and F3.

170 **Table 2. Average values of the roughness parameters (8 samples are gathered per field and per direction).**

		F1		F2		F3	
		h_{rms} (cm)	L (cm)	h_{rms} (cm)	L (cm)	h_{rms} (cm)	L (cm)
2016-2017	Parallel	0.92	5.02	1.19	5.77		
	Perpendicular	1.34	5.88	1.19	5.8		
	Average	1.13	5.45	1.19	5.78		
2017-2018	Parallel	0.89	5.44	1.1	5.88		
	Perpendicular	1.16	7.4	1.12	6.6		
	Average	1.02	6.42	1.11	6.24		
2018-2019	Parallel					0.83	6.54
	Perpendicular					0.96	7.32
	Average					0.89	6.93

171

172 Based on the range of h_{rms} measurements ($0.83 < h_{rms} < 1.35$), it can be clearly seen that the fields are characterized by a

173 slightly rough or smooth surface, which is the general case of disk tilling fields. After sowing, there is no soil work and

174 hence the change of h_{rms} and L are limited apart from the beginning of the crop season (December 28,2017, see Fig. 4). At

175 that time, the soil has just been prepared for sowing and rows are still clearly visible in the field explaining the differences

176 between both directions. This anisotropy disappeared quickly with irrigation, rainfall and plant growth.
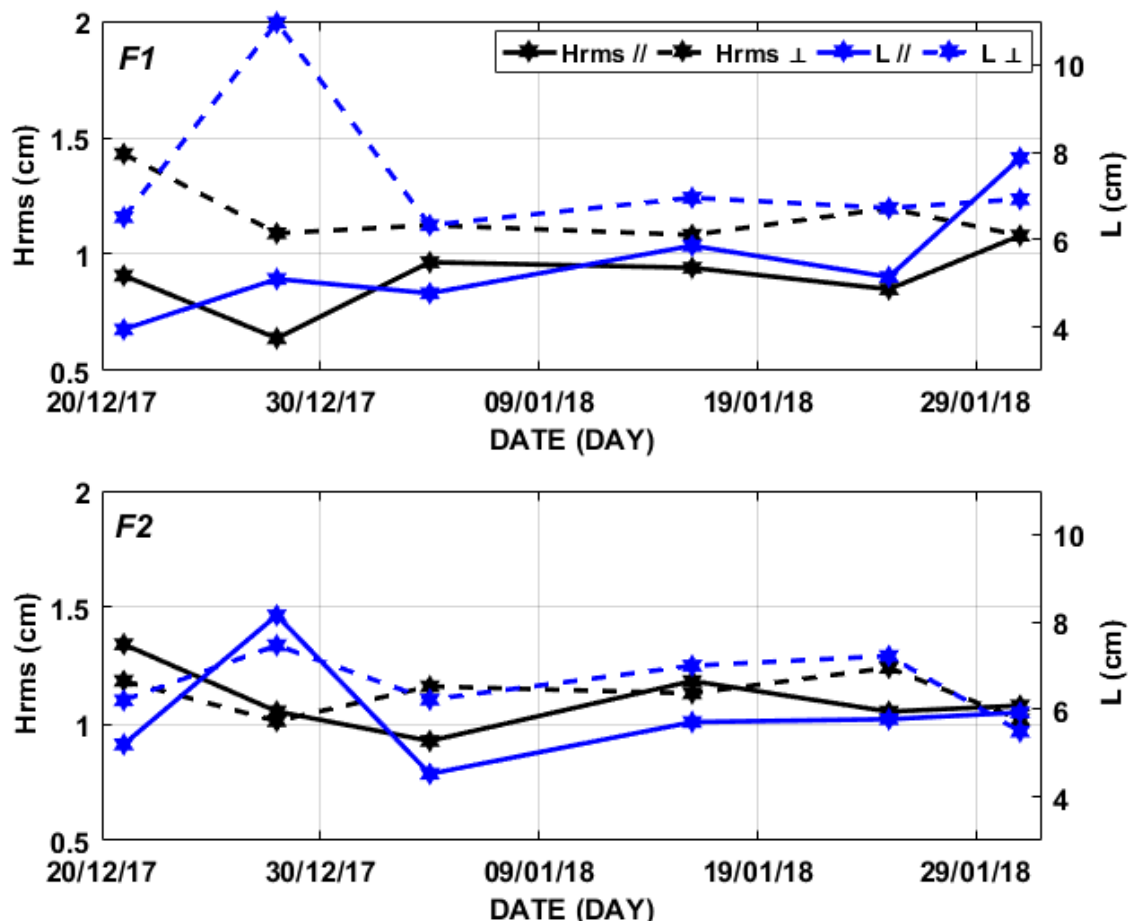
Figure 4. Time series of h_{rms} and L computed from parallel and perpendicular measurements separately for F1 and F2 during the season 2017-2018.

3.1.3 Biomass and water content

Biomass and water content are two biophysical parameters of crucial importance in different agricultural applications including particularly plant stress monitoring, backscatter, crop yield and evapotranspiration modeling. Within each field, eight samples are collected once a week/two weeks during the growing season. The samples are chosen randomly so that the average is representative of the plot. A quadrates of an area of 0.0625 m^2 is used for the sampling (Fig. 5). The samples are weighed first in the field to get fresh above-ground biomass (FAGB). The corresponding above ground biomass (AGB) expressed in kg of dry matter by m^2 is determined at the laboratory by drying the samples in an electric oven at 105°C for 48 hours. The vegetation water content (VWC) is thus computed as the difference between FAGB and AGB.

188

Figure 5. Photo taken during a measurement campaign illustrating a sample of above-ground biomass measurement.

190 **3.1.4 Canopy height, green leaf area index and cover fraction**

191 Canopy height (H), green leaf area index (GLAI) and cover fraction (F_C) are measured every week during the growing

192 season. Values from eleven different places are averaged and considered as a representative measure of the field. H is simply

193 measured using a measuring tape while GLAI and Fc are computed by processing hemispherical photos (Fig. 6b) using

194 MATLAB software. The eight photos per date and per field are taken using a camera Canon 6EOS 600D with SIGMA 4.5

195 mm F2.8 EXDC circular fisheye HSM (Fig. 6a). Photos are taken in optimal lighting conditions to avoid shadow effects and

196 over-exposure phenomena which make classification more difficult. The algorithm is based on the binarization of the

197 hemispherical images by thresholding a greenness index. Next, the useful part of the images is extracted by masking the

198 operator and the high viewing angles (> 75°) (Fig. 6c). Finally, the ground-covered area is extracted on concentric rings

199 associated with fixed viewing angles and the average of all pictures is the field GLAI. Using the same process, Fc is

200 calculated as the ratio of the vegetation pixels number to the pixels total number.

201
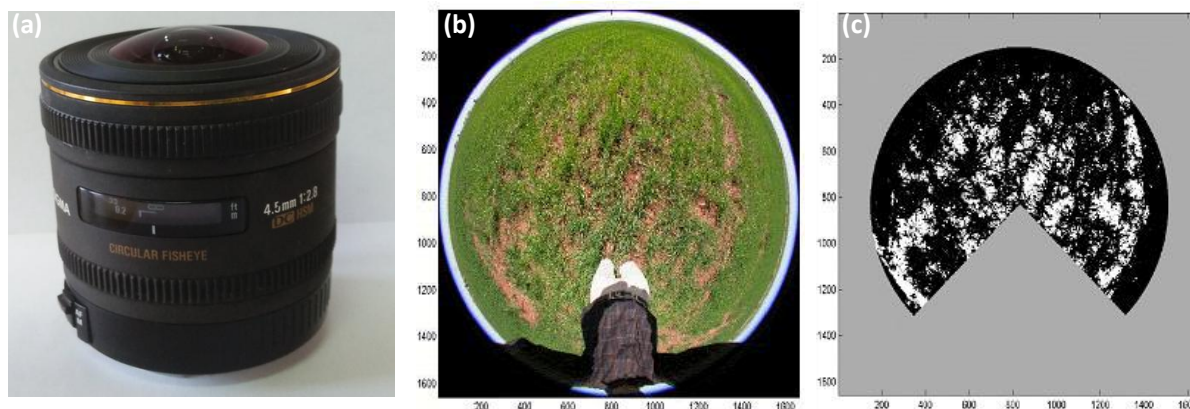
Figure 6. (a) the 4.5 mm F2.8 EXDC circular fisheye HSM, (b) hemispherical photo and (c) result of the processing after binarization and after masking the operator and the high viewing angles (> 75°).

3.1.5 Irrigation and weather data

F1, F2 and F3 are irrigated using the drip technique. Irrigation quantities are determined by the farmer by estimating the daily potential evapotranspiration (ET_p) in the region computed using the FAO-56 model (Allen et al., 1998). Irrigation is then planned on the basis of each period by giving the cumulative ET_p during that period. The irrigation pipes are spaced by 0.7 m while the distance between the drippers along the pipe is 0.4 m. Over F1 and F2, the flowrate of each dripper is 7.14 mm/hour. The irrigation takes place about 105 min (12.53 mm). A flowmeter mounted downstream of a valve allowed an accurate collection of irrigation volumes. F2 and F3 are irrigated according to FAO recommendations while F1 is stressed voluntarily. The stress involved in F1 is during the first season (2016-2017) only. By contrast, the 2017-2018 season was wet so that there is no clear stress observed on the field. The irrigation dates and amounts over F1 and F2 during both seasons are made available throughout this database while irrigation over F3 are not available.

The weather data including precipitation, air temperature, relative humidity, solar radiation, wind speed and direction are collected by an automatic weather station installed over an alfalfa field near the studied fields (Fig. 7). The weather station provides continuously meteorological data every 30 min. The sensor Campbell CS215 is used to measure the air temperature and the relative humidity (Fig. 7). The global solar radiation and the wind direction and speed are measured using Campbell SKP215 and Campbell windsonic4, respectively. The precipitation are measured using the Rain Gauge (Campbell SBS500) shown in Fig. 7.

11

220
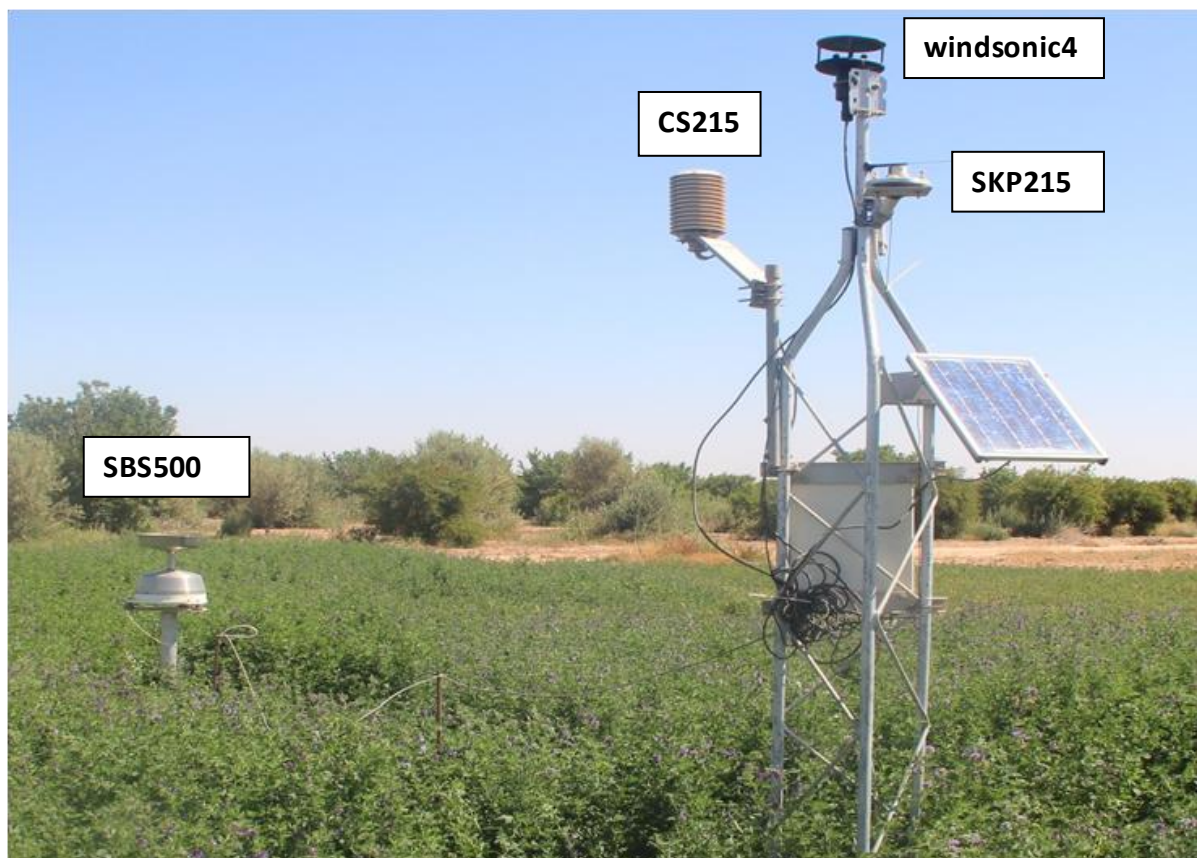
Figure 7. Automatic weather station installed over an alfalfa field near F1, F2 and F3.

222 **3.2 Remote sensing datasets**

223 **3.2.1 Sentinel-1**

224 Sentinel S1A and S1B are earth observation satellites developed for the Copernicus initiative and launched by the European

225 Space Agency on April 2014 and 2016, respectively. During full operation, S1A and S1B are maintained in the Near-polar

226 Sun-synchronous orbit at 693 km altitude, phased 180°, providing a revisit time of six days (Torres et al., 2012). S1 is a

227 synthetic aperture radar operating at C-band with a frequency of 5.33 GHz, mapping the entire world in 175 orbits per cycle.

228 The main operational imaging mode is the Interferometric Wide-swath mode (IW). IW acquires data with a wide swath of

229 250 km with high geometric (azimuth resolution 20 m and ground range resolution 5 m) and radiometric resolution (Mission

230 and Services, 2012). IW mode supports operation in single and dual polarization (HH, VV, HH/HV and VV/VH) and covers

231 a range of incidence angles between 31° and 46°. The product is composed of three Sub-Swath acquired in TOPSAR

232 imaging technique which significantly reduces the scalloping effect (Zan and Guarnieri, 2006).

233 Level 1 products are systematically processed and available within 24 hours, free of charge from the Sentinel-1 Data Hub

234 website (https://scihub.copernicus.eu). The website provides data under two types of products: GRDH (Ground Range

235 Detected High resolution) and SLC (Single Look Complex).

236 In this database, 561 GRDH and SLC products are processed (Table 3). Among them, 124 images are acquired over F3

237 during 2018-2019 growing season and 437 over F1 and F2 from October 01, 2016, to July 31, 2018, along the ascending

238 #118 (221 images) and descending #52 (216 images) relative orbits. This period includes two agricultural seasons in addition

239 to the summer period.

240 **Table 3. Characteristics of the sentinel-1 products processed over the three fields for the monitored periods**

Field	Season	Relative Orbit Number	Incidence angle	Relative Orbit	Overpass time	Product	Number of images
F1 and F2	October 2016 - July 2018	118	45,6°	Ascending	18:30	GRDH	112
						SLC	109
		52	35,2°	Descending	06:30	GRDH	110
						SLC	106
F3	November 2018 - May 2019	118	45,6°	Ascending	18:30	GRDH	32
						SLC	31
		52	35,2°	Descending	06:30	GRDH	31
						SLC	30

241 *Backscattering coefficient*

242 GRDH products are provided by ESA with a square pixel size and contains only the intensity information. The

243 backscattering coefficients are extracted using the Orfeotoolbox (CNES, 2018). The processing procedure consists of three

244 steps:

245 1. *Thermal noise removal*: SAR product contains not only the useful signal but also the unwanted noise disturbing the

246   information contained in the intensity images, especially when the backscattered power is low. The thermal noise is

247   an additive noise. The compensation of this noise can be performed by subtracting the scaled noise power using the

248   calibrated noise vectors provided by ESA.

249 2. *Calibration*: The "calibration" step aims to convert the digital accounts into a physically interpreted parameter: the

250   backscattering coefficient. A calibration vector included in the GRDH products contains the necessary information

251   to convert the digital values to the backscattering coefficient.

252 3. *Terrain correction*: S1-SAR data are sensed with viewing angle greater than zero which induces distortion in the

253   products because of the lateral viewing geometry. The "Terrain corrections" module is used to compensate these

254   distortions and get as much possible images with the real geometric representation. The images are projected on the

255   Earth's surface using a Digital Elevation Model (DTM). The DTM SRTM (Shuttle Radar Topography Mission) of
256   30 m of resolution is used according to the method described in Small and Schubert (2008).

257 SAR images are affected by the speckle noise, which is mainly due to the relative phase of individual scatters within a
258 resolution cell. Many filters have been developed to remove the speckle noise although the best filter is the spatial average.
259 The presented database is generated using a simple average per field. In order to visualise data dynamics, backscattering
260 coefficients are converted into dB.

261 *Interferometric coherence*

262 Sentinel-1 SLC products are provided in slant-range geometry. It contains three sub-swath images IW1, IW2 and IW3. Each
263 sub-swath is composed by nine bursts with black-fill demarcation. By contrast with GRD, both intensity and phase
264 information are kept. The phase information is used for the computation of interferometric coherence. SAR interferometry
265 consists of correlating two images acquired from two positions in space slightly separated from each other (with two radars
266 mounted on the same platform) or at different times by exploiting repeated orbits of the same satellite such as for Sentinel-1.
267 Thanks to its high temporal resolution (six days per orbit), the interferometric coherence is computed from two consecutive
268 acquisitions of the same orbit.

269 The interferometric coherence, given by the Eq. (2), for a local neighborhood of N pixels, is generated by cross multiplying,
270 pixel by pixel, the first SAR image z_i with the complex conjugate $z_i'^*$ of the second (Bamler and Hartl, 1998; Touzi et al.,
271 1999).

272

273
$$\rho = \frac{\sum_{i=1}^{N} z_i \cdot z_i'^*}{\sqrt{\sum_{i=1}^{N}|z_i|^2 \cdot \sum_{i=1}^{N}|z_i'|^2}} \tag{2}$$

274 The interferometric coherence $|\rho|$ varies between zero (incoherence) and one (perfect coherence). The interferometric
275 coherence is related to the movements of the scatterers within a given canopy. It decreases (loss of coherence) in the case of
276 dense vegetation while high values are obtained over bare soils. Loss of coherence could be caused by temporal interval
277 between acquisitions, orbit errors, vegetation development/movement or processing errors. The random dislocation of
278 scatters because of the weather (wind and rain) or the plants growth is the main cause of the temporal decorrelation.

279 Sentinel application platform SNAP is used to compute the interferometric coherence from S1-SLC products in five steps:

280   1. *Apply-Orbit-file*: This module is applied for a better estimation of the position and speed of the satellite using the
281   orbit state vector. Preliminary, a predicted orbit state vector is contained in the metadata but it is not accurate. The
282   precise orbit is made available one month after data acquisition at the later. For this reason, the automatic download
283   in SNAP is used in order to update the orbit state vectors.

284   2. *Back-geocoding*: The two images need to be co-registered. One of the images is the master and the other is the
285   slave. This step ensures that each pixel of the slave image is aligned with the corresponding pixel in the master

286   image so that both pixels contain contributions from the same target. The DEM is required for "*Back-geocoding*"

287   step, SNAP allows either to enter it manually or to download it automatically.

288   3. *Coherence*: This module in SNAP allows the computation of the interferometric coherence between the two images

289   for a given local neighborhood. In order to get a square pixel of 13.95 m, azimuth* range are fixed to 3*15 in the

290   processing.

291   4. *TOPSAR-Deburst*: The black-fills in between bursts are deleted separately for both polarization images (VV and

292   VH).

293   5. *Terrain-Correction*: Finally, the processed images are projected on the earth surface using a DEM.

3.2.2 Sentinel-2 NDVI

295 Sentinel-2 optical satellites S2A and S2B are launched by ESA in June 2015 and March 2017, respectively. They are placed

296 in opposition on the same orbit at an altitude of 800 km. Sentinel-2 provides data every 5 days with a width of 290 km and a

297 resolution of 10 to 60 m according to spectral bands (13 bands) ranging from visible to the medium infrared. The National

298 Centre for Space Studies (CNES) provides Level-2A products atmospherically corrected free of charge via the PEPS

299 platform (https://peps.cnes.fr/) or the Theia website (https://theia.cnes.fr/). Data are corrected from atmospheric effects by

300 the Center for the Study of the Biosphere from Space (CESBIO) using the MAJA chain (Hagolle et al., 2015). Data are

301 downloaded from the Theia site. Among the available products, only the products non-covered with clouds are used

302 corresponding to ten, twenty-five and twenty-six images for 2016-2017, 2017-2018 and 2018-2019 agricultural seasons,

303 respectively. Please note that during the season 2016-2017, only S2A was in the orbit which explaining the limited number

304 of images (10). Next, the Normalized Difference Vegetation Index (NDVI) corresponding to each pixel is computed from

305 band 4 and 8. An average per field is used to compute the time series of each field.

4 Data analysis

4.1 Vegetation variables

308 In this section, the relationships between the different variables (GLAI, FAGB, AGB, VWC and H) that characterize the

309 vegetation growth and development are firstly investigated. These relationships are extensively used for different

310 applications such as the calibration of backscattering models and the development of retrieval approaches (Chauhan et al.,

311 2018). Several land surface or crop model relies on empirical relationships to predict Fc or H as well (Bigeard et al., 2017;

312 Castelli et al., 2018). Other agricultural models compute AGB from GLAI using linear or polynomial relationships (Major et

313 al., 1986; Petcu et al., 2003). Figure 8 displays the resulting relationships using data from F1 by selecting only the 2016-

314 2017 season for illustration purposes. These relationships are computed separately based on the data recorded before and

315 after the peaks of GLAI and FAGB.

316   The nature of the relationship changes depending on the structure (biomass variables) or on the greenness of the plant

317   (GLAI). The biomass variables (FAGB, AGB and VWC) and H increase up to the biomass peak. Afterwards, are verse

318   evolution can be observed characterized in particular, by a decorrelation between FAGB/VWC and AGB. This is mainly

319   related to the senescence process of the vegetation; the leaves begin to dry progressively with the start of the grain filling, so

320   that the Sapflow (water, carbohydrates, proteins and mineral salts)migrates to the heads at the top of the plant (Farineau and

321   Morot-Gaudry, 2018). Indeed, VWC and AGB are highly correlated until vegetation peak (the correlation coefficient R =

322   0.94 before the peak and R = -0.20 afterwards) while FAGB being dominated by the plant water content is highly correlated

323   with VWC during the whole crop season (R=0.99 before the peak and R = 0.98 afterwards). Likewise, H is highly correlated

324   to FAGB, VWC and AGB until vegetation peak (R > 0.97) when H remains at its maximum value while AGB continue to

325   increase with grain filling and VWC and FAGB decrease because of the vegetation drying. The relationship of these

326   variables (FAGB, AGB, VWC and H) with GLAI and Fc is quite different. The curves are of a parabolic shape with a

327   maximum reached around the GLAI peak. A timing shift between the peaks of GLAI and FAGB is observed. This is

328   probably related to the senescence of the lower leaves, which leads to an earlier drop of GLAI than of FAGB. Between the

329   peaks of GLAI and FAGB, GLAI decreases while i) AGB and H increase and ii) FAGB increases slightly while VWC is

330   almost constant. After the FAGB peak, AGB goes on increasing due to grain filling while the VWC decreases due to drying

331   of the plant. FAGB which is the sum of AGB and VWC is almost constant.
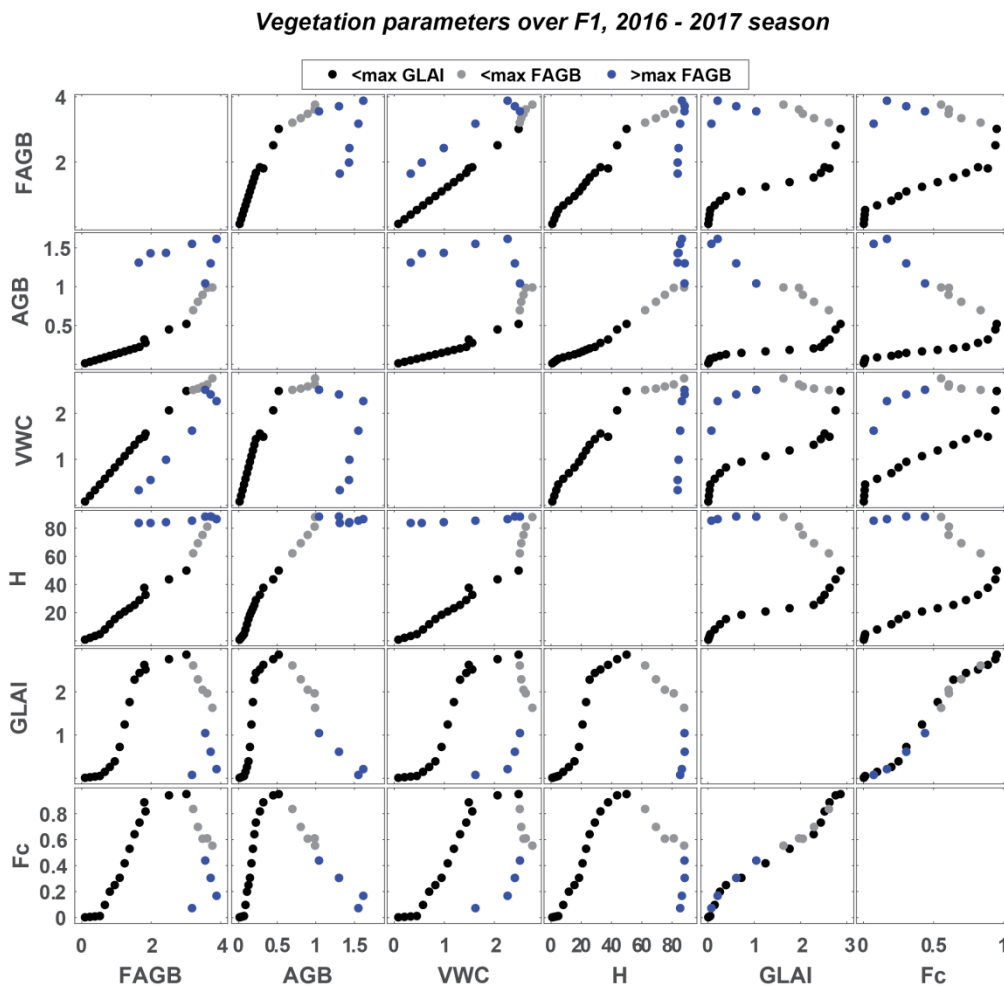
Figure 8. Scatterplots of the relationships between wheat measured variables: FAGB, AGB, VWC, H, GLAI and Fc. Data are presented separately using the maximum of GLAI and FAGB as thresholds: data <max GLAI are in black, data < max FAGB (and > max GLAI) are in grey and data > max FAGB (and > max GLAI) are in blue.

4.2 Radar data

The time series of the backscattering coefficient, the polarization ratio and the interferometric coherence are analyzed here for two agricultural seasons and a summer period on F1 and F2 and at two incidence angles (35.2° and 45.6°).

4.2.1 The backscattering coefficient

Figure 9 displays the time series at 45.6° over F2 for illustration purposes: a) backscattering coefficient at VV polarization (σ_{VV}^0); b) backscattering coefficient at VH polarization (σ_{VH}^0) as well as wheat phenological stages; c) SSM, air temperature,

17

342   irrigation and rainfall. Figures A3- A5 in appendix A show the same time series over F1 and F2 at 35.2° and F1 at 45.6°,

343   respectively. The backscattering coefficients reveal a strong seasonal signal with two cycles. The first cycle takes place from

344   sowing to the heading stage and the second from heading to harvest with the minimum reached around the heading stage.

345   The highest values at 35.2° are observed in the first cycle, while at 45.6°, σ° is higher on the second peak. The maximum

346   values of σ_{VV}^0 reached the same value for F1 and F2 while higher values are observed on F2 at VH. σ_{VV}^0 is more sensitive to

347   soil moisture variation until mid-January, corresponding to the tillering stage, when the soil is not yet fully covered by

348   vegetation. The signal hereafter decreases gradually from the early tillering until the heading stage (around March 13) by

349   about 10 dB on F2 and 5 dB on F1 because of the attenuation by the canopy during the development of the stems (extension

350   stage). Obviously, the attenuation is more important at VV polarization because of the vertical structure of wheat (stems) in

351   line with the results of (Fontanelli et al., 2013; Picard et al., 2003; Wang et al., 2018). The response of σ_{VH}^0 to SSM variation

352   and canopy attenuation is lower than for σ_{VV}^0. After the heading stage, the signal starts to increase again. This is clearer on F2

353   than F1 and at 45.6° than at 35.2°. The heading stage is the phenological stage of wheat when the spike or head starts

354   emerging out from the leaf sheath. This change of the structure of the canopy shield the stems for the radar signal through

355   the appearance of a thick, wet top layer composed of the heads. The C-band wavelength penetrates this layer only, resulting

356   in increased volume scattering, while attenuation becomes low (Brown et al., 2003; El Hajj et al., 2019; Mattia et al., 2003;

357   Patel et al., 2006; Veloso et al., 2017). This effect is stronger for F2 than for F1, at VH than at VV and at 45.6° than at

358   35.2°. The exceptional growing conditions on F2 during S2 is at the origin of the observed plateau of the backscattering

359   coefficient which remains quite stable until harvest. This is due to a significant contribution of volume scattering which is a

360   behavior that characterize a crop developing a random canopy structure in relation to the numerous and dense adventices as

361   already highlighted (cf. picture Fig. A1 at appendix A).

362   The low variation observed on F1 during the 2016-2017 season is mainly related to the limited development of vegetation

363   because of the triggered water stress. Likewise, the difference between the two seasons over F2 is related to a higher density

364   of grown seeds and wetter conditions in the 2017-2018 season compared to 2016-2017 (the amount of rainfall during the

365   growing season-from sowing to harvest-reached 167.23 mm in 2017-20118 while only 69.94 mm is recorded in 2016-2017).

366   With the drying of the head layer, the backscattering decreases again at the end of the season to reach the lower observed

367   values. Indeed, as the head layer dries, the vegetation becomes transparent to the signal. The soil is also dry at the end of the

368   season because irrigation is stopped. These low values remained until the first deep ploughing on July 11, when a sharp

369   increase is observed because of a drastic change of soil roughness. Hereafter, the signal is again stable until the seedling

370   preparation work for the next 2017-2018 season (November 22).
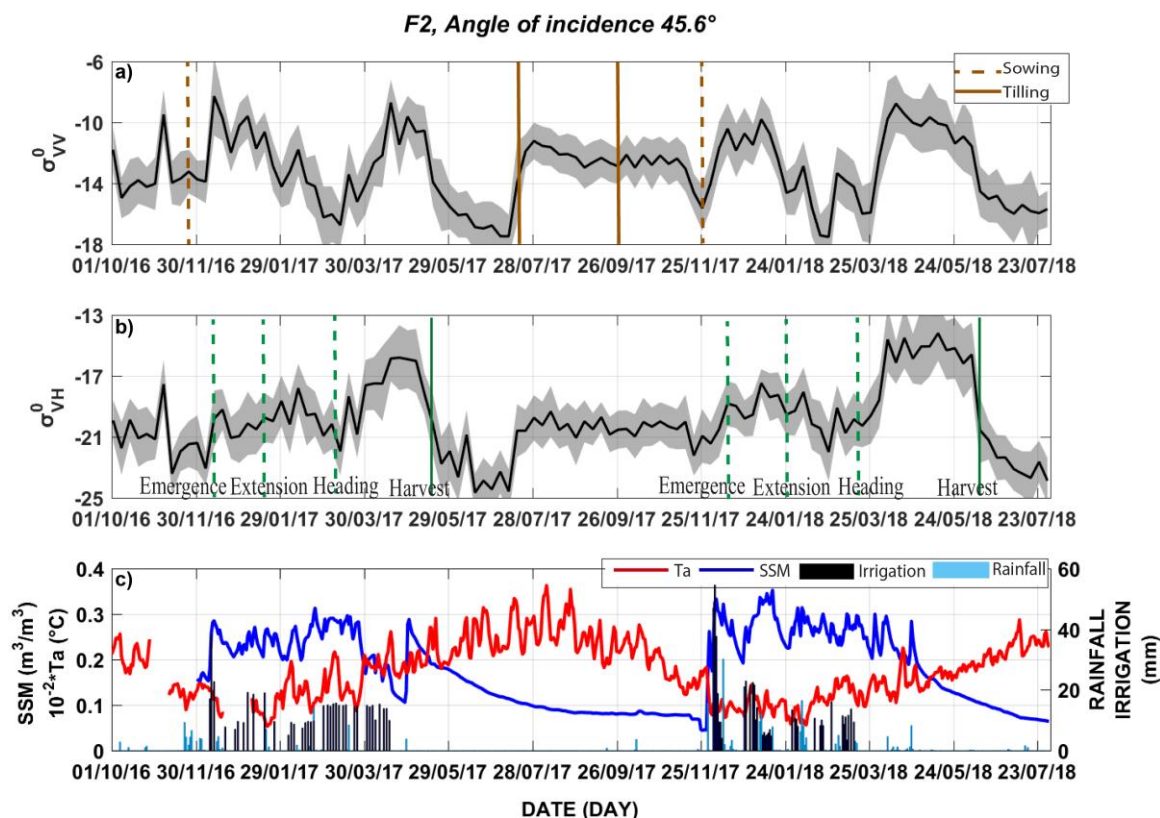
Figure 9. Time series of the backscattering coefficient at VV (a) and VH (b) polarizations on F2 at 45.6° of incidence angle during the period from October 01, 2016 to July 31, 2018. The tilling works and phenological stages of wheat are superimposed on subplots (a) and (b), respectively. The air temperature, surface soil moisture (SSM), irrigation and rainfall are displayed on subplot (c).

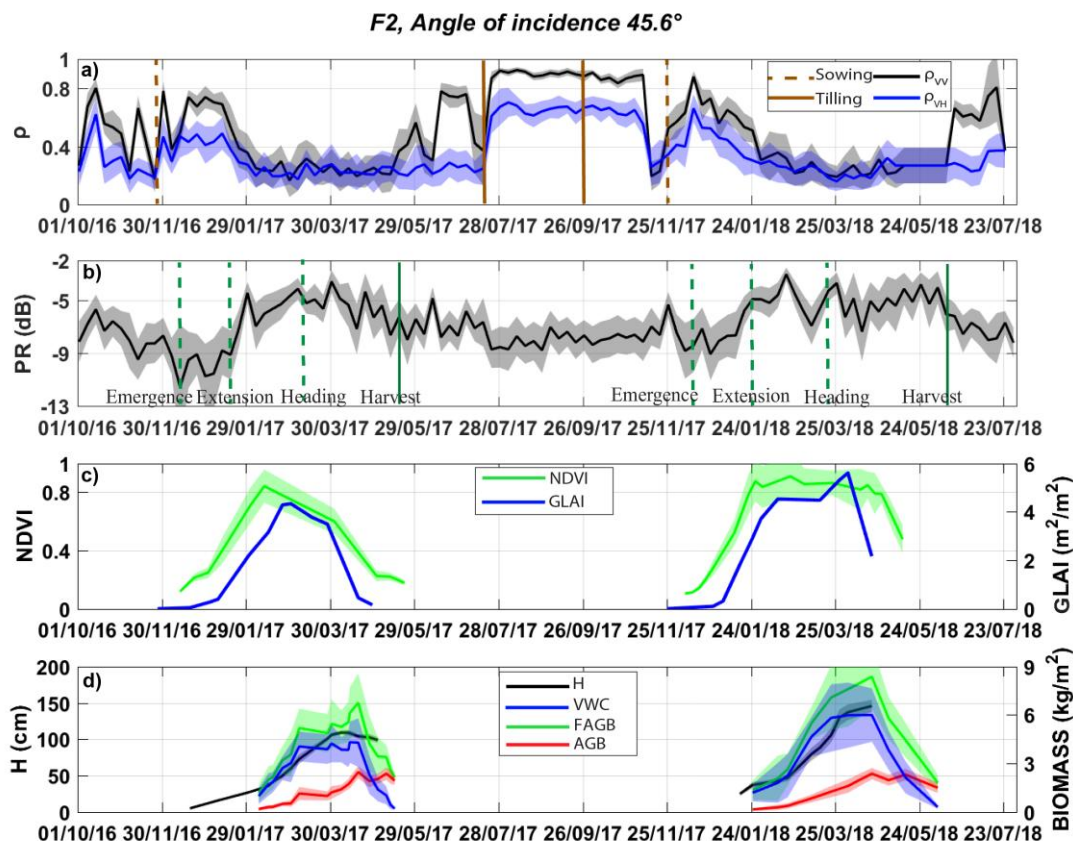**4.2.2 The interferometric coherence and the polarization ratio**

Figure 10 displays the time series at 45.6° over F2 of: a) interferometric coherence at VV (ρ_{VV}) and VH (ρ_{VH}) polarizations together with sowing and tilling dates; b) polarization ratio (PR), as well as wheat phenological stages; c) Sentinel-2 NDVI and measured GLAI; d) Measured FAGB, AGB, VWC and H. Likewise, Fig. A6- Fig. A8 in appendix A display the time series over F1 and F2 at 35.2° and F1 at 45.6°, respectively. The time series of ρ_{VV} and ρ_{VH} follows a similar evolution. Before sowing, coherence is at its highest value corresponding to 0.9 for ρ_{VV} and 0.7 for ρ_{VH} (Fig. 10a). These values express a dominance of coherent scattering, corresponding to response of bare soils composed of big rocks. Indeed, during the summer, the plots are subjected to deep ploughing which yields big clods that resist any change in surface structure caused by climatic factors such as wind or rain. The second tilling breaks up the clods for the next seeding. Soil works and farming activities induce a large decrease in coherence in line with the observation of Wegmuller and Werner (1997). The

19

386   surface roughness is a main parameter that influences not only the amplitude at C-band but also the phase. Indeed, abrupt

387   drops are observed around each sowing events and tilling works (brown vertical lines on Fig. 10a).

388   After sowing, the interferometric coherence increases from 0.15 to 0.7 and then starts to decrease slightly from the

389   emergence of wheat, becoming almost constant after stem extension with values < 0.3 corresponding to the noise level.

390   Actually, the interferometric coherence is known to decrease exponentially with wheat growth (Lee et al., 2012). Vegetation

391   growth and random dislocation of scatters cause a degradation of coherence (Blaes and Defourny, 2003; Engdahl et al.,

392   2001; Wegmuller and Werner, 1997), especially under wind and rain effects. Between sowing and emergence, the observed

393   variation is assumed to be related to the installation of irrigation drippers that took place up to two weeks after sowing. The

394   changes that occur between the harvest and the first tilling could be attributed to livestock grazing, a common practice in the

395   region after wheat harvest, which could change the surface roughness.

396   The polarization ratio (PR) is closely related to the biomass dynamic. Both are increasing from emergence to heading and

397   then start to decrease until harvest. The maximum timing is around middle of April. The significant differences in

398   biophysical parameters between F1 and F2 is due to irrigation, as already highlighted for the backscattering coefficient time

399   series. Likewise, the difference between the two seasons over F2 is related to a higher sowing density and wetter conditions

400   in the 2017-2018 season compared to 2016-2017. As shown above (Fig. 8), the time series of FAGB and VWC are in line

401   with AGB and H up to the peak of FAGB and then decrease together while AGB continues to increase and H remains at its

402   maximum value. FAGB and VWC are dropping at the same time but 50 days after when compared to GLAI and NDVI and

403   about 15 days before the backscattering coefficient.

Figure 10. Time series of the interferometric coherence at VV and VH polarizations (a) and the polarization ratio (b) on F2 at 45.6° of incidence angle during the period from October 01, 2016 to July 31, 2018. The tilling works and phenological stages of wheat are superimposed on subplots (a) and (b), respectively. NDVI and measured GLAI are displayed in subplot (c). Measured H, FAGB, VWC and AGB are plotted in subplot (c). Time series are presented by mean values (solid lines) and standard deviations (filled fields surrounding the solid lines).

4.3 Relationship between SAR data and vegetation variables

The polarization ratio and the interferometric coherence have been shown to be related to vegetation growth. In this section, the relationships between PR, ρ_{VV} and ρ_{VH} and vegetation variables, including AGB, VWC, H, GLAI and NDVI are analyzed. Figure 11 displays the results at 35.2° of incidence angle and Fig. A9 in appendix A displays the results at 45.6°. H is used to illustrate the vegetation growth because its evolution is monotonic, so that data corresponding to before and after maximum development can be easily separated. The determination coefficient R^2 and the Spearman rank correlation Rs are superimposed on the subplots together with the fitting equations using the whole database. Overall, a good correlation has been found between SAR variables (PR, ρ_{VV} and ρ_{VH}) and AGB, VWC, GLAI and H. A hysteresis behavior is obviously observed for the vegetation variables with a non-monotonic dynamic (VWC, NDVI and GLAI). Using PR, the relationships are more scattered and characterized by lower saturation value. Although the range of variation of ρ_{VH} is limited with

420 regards to PR, the statistical metrics of the relationships between interferometric coherences and the vegetation variables are
421 better than those obtained using PR. ρ_{VV} exhibited better correlation to the vegetation variables than ρ_{VH}. With the exception
422 of NDVI, Rs is always greater than 0.67. The best fit is obtained between ρ_{VV} and H (Rs = 0.78 and R^2 = 0.65) with higher
423 saturation value than the other relationships (~55% of H range which is about 77 cm). By contrast, a visual inspection of the
424 Fig. 11 (d, i and n) shows that relationships with NDVI are poorer when using data of the whole growing season. The
425 dispersion is strong along the season. Data before and after the maximum development can be distinguished, particularly,
426 using ρ_{VV} and to a lesser extent ρ_{VH}. Figure 11 (i and n) shows that a linear relationship exists between NDVI and SAR data
427 using data before maximum development only, i.e. when the vegetation is still green. During the beginning of the season, the
428 slope of ρ_{VV}-NDVI and ρ_{VH}-NDVI is low compared to the other vegetation variables. This is because the NDVI increases
429 faster around the emergence of wheat while ρ_{VV} is steel high because of the low vegetation cover fraction at this time. The
430 hysteresis effect observed after the maximum of vegetation development is due to the senescence of the leaves when NDVI
431 starts decreasing while ρ_{VV} and ρ_{VH} are stable at low values.

432 When considering SAR data at 45.6° of incidence angle (Fig. A9), a similar behavior to Fig. 11 is observed with AGB,
433 VWC, H and NDVI. Same hysteresis and scattering are observed for NDVI although higher correlations are obtained.
434 Similarly, ρ_{VV} is better correlated to vegetation parameter than ρ_{VH} and PR. By contrast, GLAI is better correlated with SAR
435 variables than H. The PR-GLAI relationship is more scattered than at 35.2° while ρ_{VV}-GLAI has the best metrics (Rs = 0.82
436 and R^2 = 0.73) with a higher saturation value around 50% of the GLAI range (3 m^2 m^{-2}).
437 Unlike PR, the metrics at both 35.2° and 45.6° are stable for the relationships between ρ_{VV} with AGB, VWC and H. By
438 contrast, PR-GLAI is more stable than ρ_{VV}-GLAI at both incidence angles.
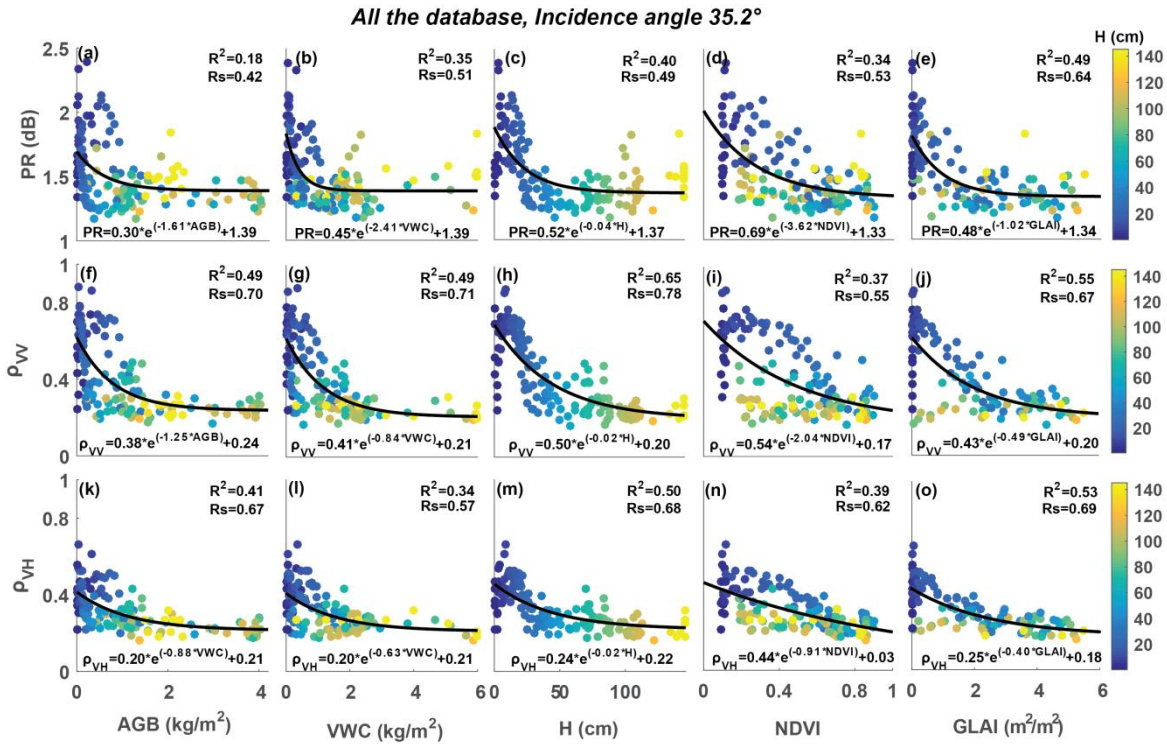
Figure 11. Scatter plots of the relationships between PR, ρ_{VV} and ρ_{VH} and AGB, VWC, H, NDVI and GLAI at 35.2° angle of incidence. The entire database is used from the three fields (F1, F2 and F3). H is used to monitor the evolution during the growing season. All the determination coefficient R^2 and the Spearman rank correlation Rs are significant at 99%.

4.4 Relationship between backscattering coefficient and SSM

Figure 12 displays the relationships between σ^0 and SSM using the entire database at 45.6° and 35.2° of incidence angles. H is used as an indicator of vegetation growth. The correlation coefficient is computed separately for the entire database and for data corresponding to H lower than a threshold value (H_{tr}) correspond to GLAI < 1.5. This value of GLAI correspond to wheat not fully covering the soil (Ouaadi et al., 2020b). H_{tr} is about 23.5 cm, 23.5 cm, 32.9 cm and 26 cm for F1 and F2 during 2017-2018, for F2 during 2016-2017 and for F3. Overall, σ^0_{VV} is obviously better correlated to SSM than σ^0_{VH} in line with the results of numerous studies (Holah et al., 2005; Li et al., 2014; Ulaby and Batlivala, 1976). Likewise, metrics at 35.2° are better than those obtained at 45.6°. This is expected as the contribution of vegetation is dominant at higher incidence angles and at VH polarization. The relationships are scattered when using data from the whole season. This is attributed to the presence of vegetation and mainly to the attenuation of the soil signal backscattered by the wheat. The sensitivity of σ^0 to SSM decreases progressively during the growing season as shown by the decreasing slope of the relationships with the vegetation development. By considering the early season data only, when the soil is not yet covered by

455 vegetation, a better fitting is obtained between σ^0 and SSM. Indeed, the correlation coefficient using data with $H < H_{tr}$ is

456 improved whatever the polarization and the incidence angle. Obviously, the highest correlation is obtained at VV

457 polarization and 35.2° of incidence angle (R = 0.73) and to a lesser extent at VV at 45.6° and VH at 35.2° with R ≥ 0.66.
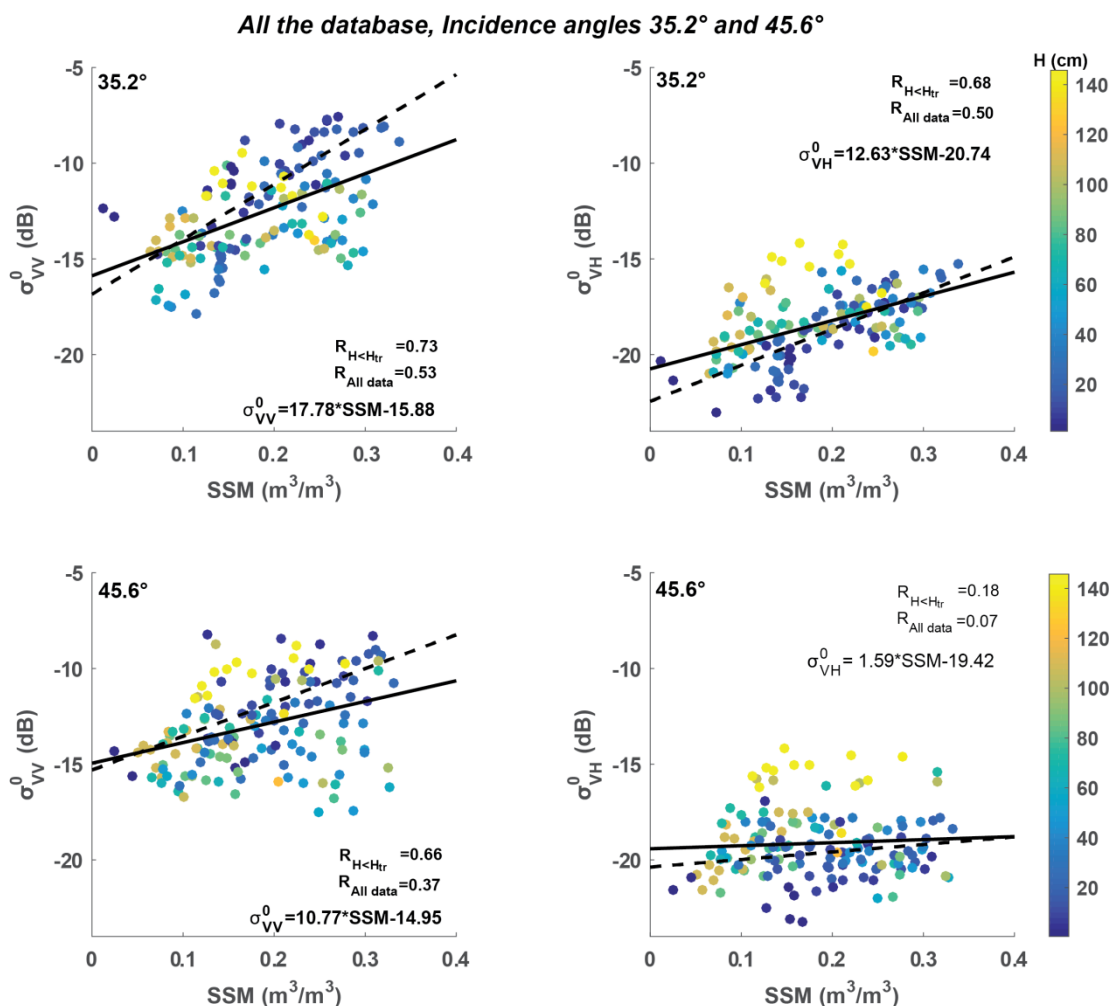
Figure 12. Scatter plots of the relationships between σ^0_{VV} and σ^0_{VH} and SSM at 45.6° and 35.2 2° angles of incidence. The entire database is used from the three fields (F1, F2 and F3). H is used to monitor the evolution during the growing season. The significant correlation coefficients are in bold. The solid and the dashed lines correspond to all database and data with GLAI < 1.5, respectively.

463   **5 Conclusion**

464   This paper presents a 3-year database of C-band radar data and all necessary ancillary ground measurements to improve our
465   understanding of the radar signal and to develop inversion methods for land surface parameters retrieval. The data are
466   collected from three heavily monitored wheat fields under semi-arid conditions in the center of Morocco. The database offers
467   a complete set of data for radar applications on wheat monitoring. The measured parameters include fresh and dry above
468   ground biomass, canopy height, leaf area index, cover fraction, surface soil moisture, root zone soil moisture and surface
469   roughness, in addition to the normalized difference vegetation index and SAR data (the backscattering coefficient and the
470   interferometric coherence). The irrigation and meteorological data are also provided. This database opens the opportunity to
471   use remote sensing together with measured parameters to understand and investigate the behavior of wheat crops and
472   thereafter for vegetation parameters and soil moisture retrieval. The database analysis presented in this paper demonstrates
473   the potentialities of SAR data for wheat monitoring by addressing the well-known sensitivity of SAR to surface soil moisture
474   and vegetation variables. The obtained relationships between SAR measurements including backscattering coefficient,
475   polarization ratio and interferometric coherence can be used for the application of several backscattering models, the
476   retrieval of biophysical variables and for yield prediction in crop models. They can also be useful for land surface models
477   relying on accurate estimation of vegetation height such as the energy balance models (i.e. TSEB -Two Source Energy
478   Balance- Norman et al., 1995). The dataset illustrates also the complex signal acquired by C-band radar over wheat crops
479   that is not yet fully understood as it mix the responses from highly dynamic contributions of soil and vegetation elements.
480   The unique dataset provided in this paper should contribute through future studies to improve our understanding of the
481   response of C-band radar observations over annual crops.

482   **6 Database availability**

483   This database is archived in DtaSuds repository of the French National Research Institute for Sustainable Development
484   (IRD). The database is accessible free of charge with "CC-BY" licence at https://doi.org/10.23708/8D6WQC (Ouaadi et al.,
485   2020a). It can be downloaded as xlsx files accompanied by a variable dictionary containing the variable names and units.
486   The files are also accompanied by a metadata including a description of the database, time coverage, keywords and other
487   general information.
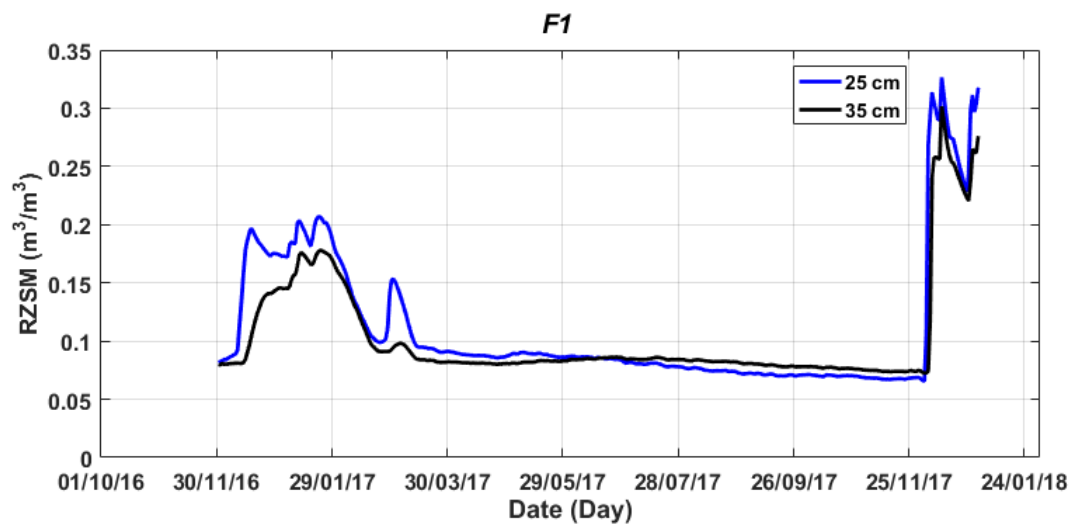488

489 **Appendix A: Complimentary figures**

490

491 **Figure A1. Picture taken over F2 during 2017-2018 growing season (14/05/2018) illustrates the specific growing conditions**
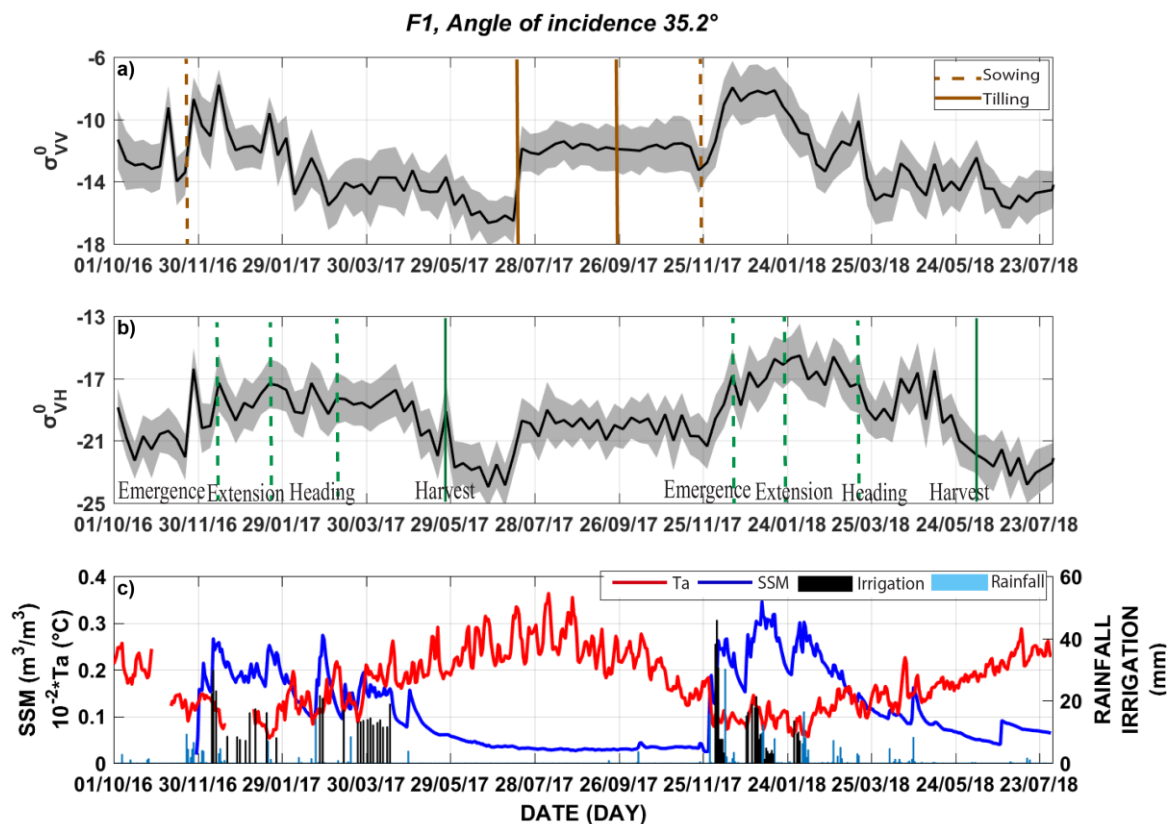492 **(adventices and stems laid down by wind).**

493

494

495 **Figure A2. Time series of root zone soil moisture (RZSM) at 25 and 35 cm of depth measured over F1 from December 01, 2016 to**
496 **December 31, 2017.**

Figure A3. Time series of the backscattering coefficient at VV (a) and VH (b) polarizations on F1 at 35.2° of incidence angle during the period from October 01, 2016 to July 31, 2018. The tilling works and phenological stages of wheat are superimposed on subplots (a) and (b), respectively. The air temperature, Surface soil moisture (SSM), irrigation and rainfall are displayed on subplot (c).
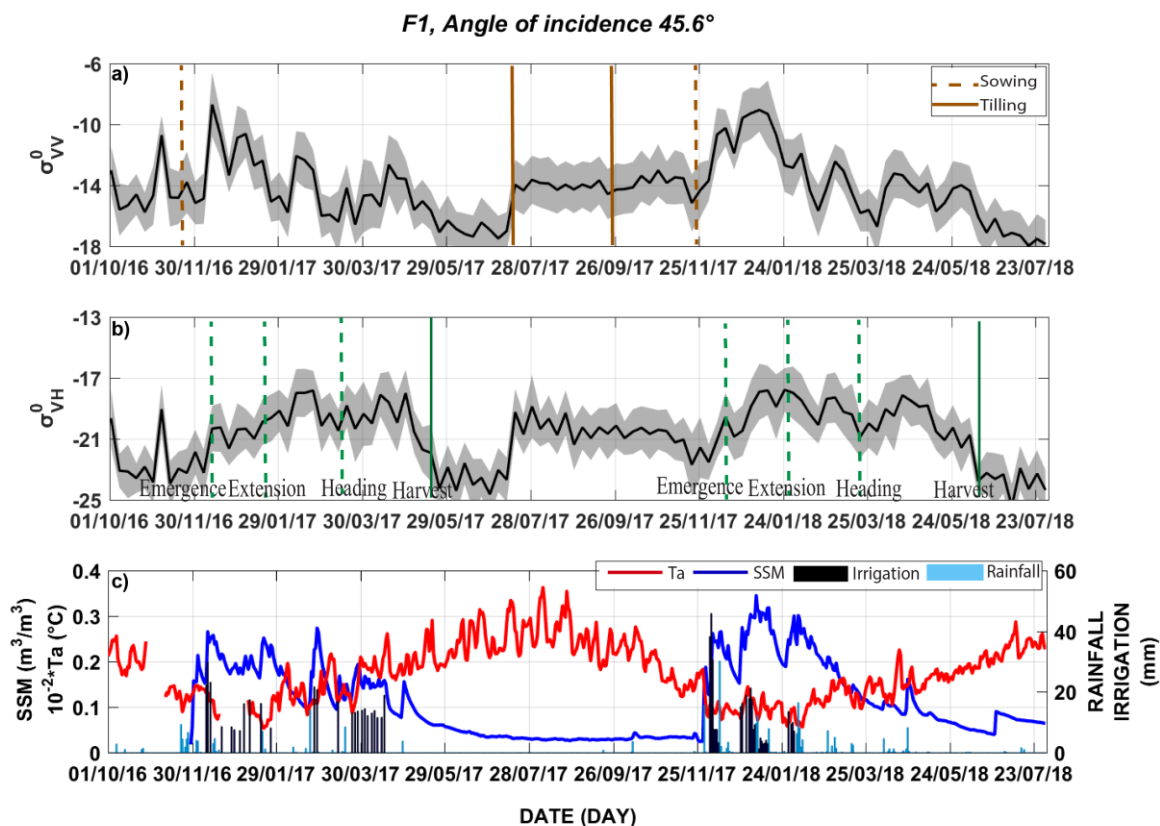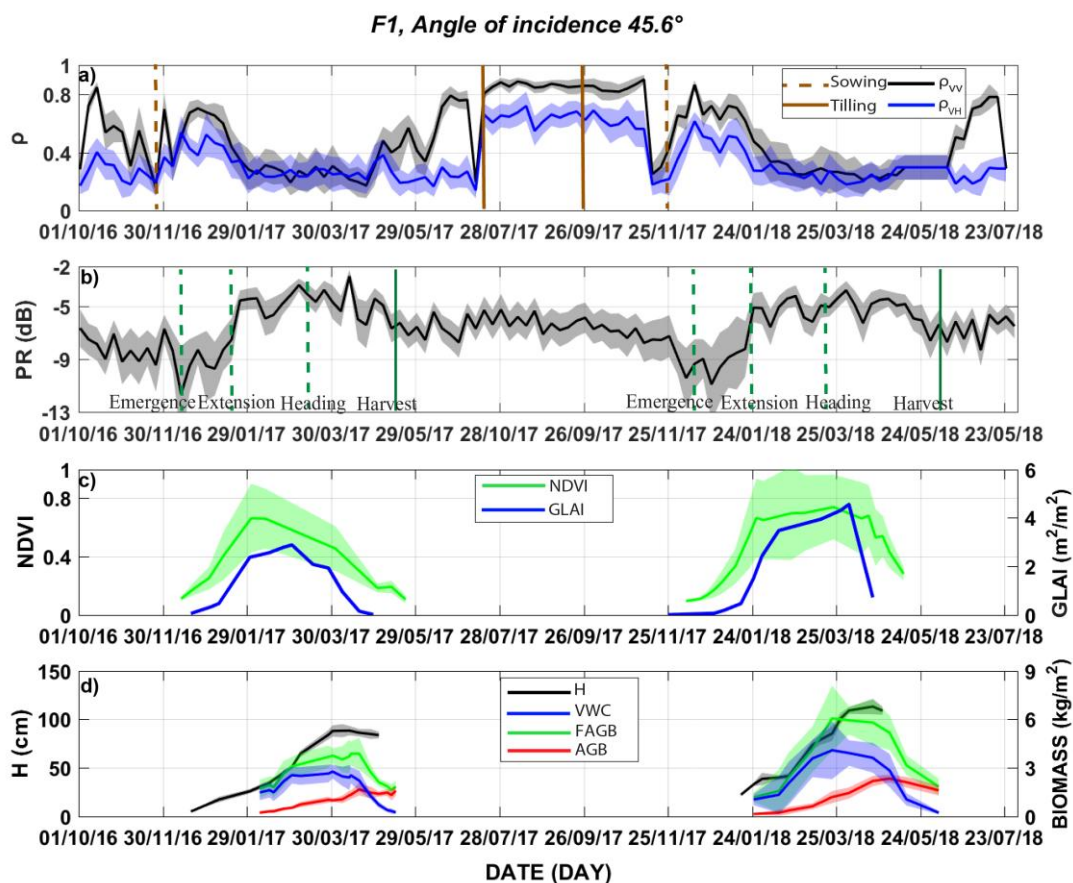
Figure A4. Time series of the backscattering coefficient at VV (a) and VH (b) polarizations on F1 at 45.6° of incidence angle during the period from October 01, 2016 to July 31, 2018. The tilling works and phenological stages of wheat are superimposed on subplots (a) and (b), respectively. The air temperature, Surface soil moisture (SSM), irrigation and rainfall are displayed on subplot (c).
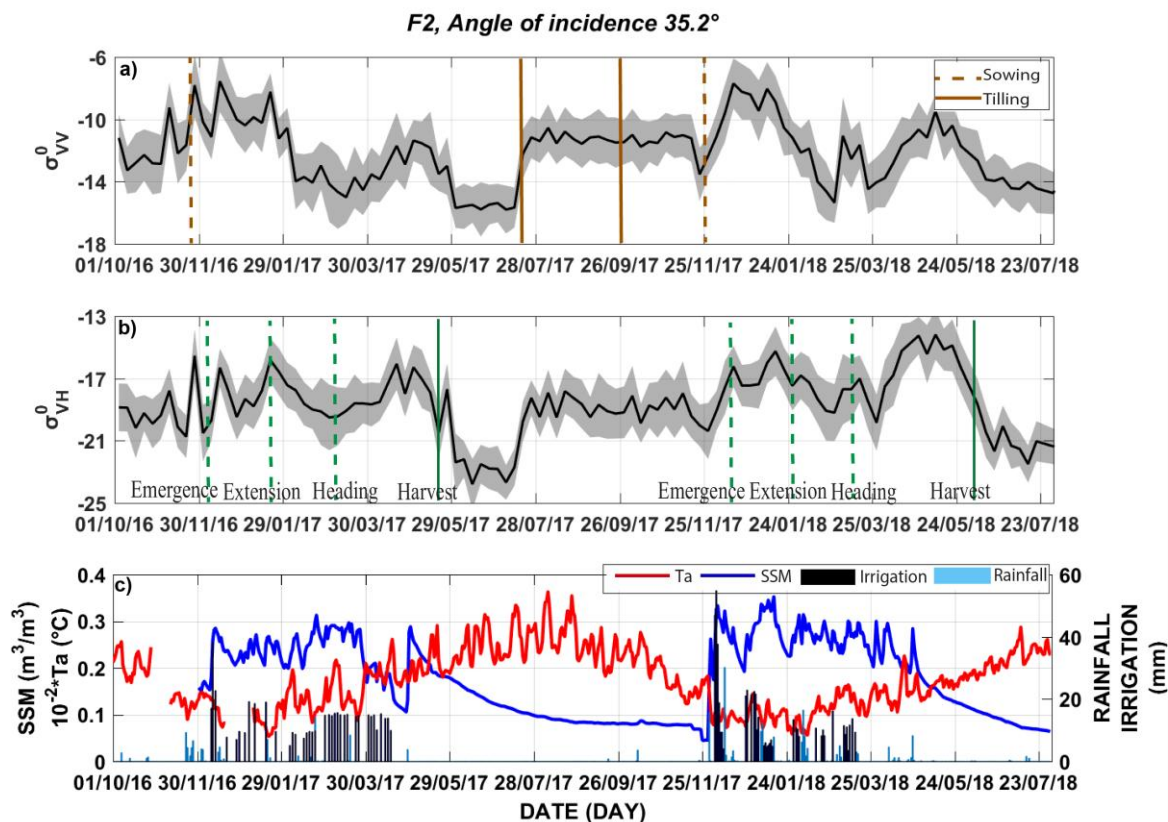
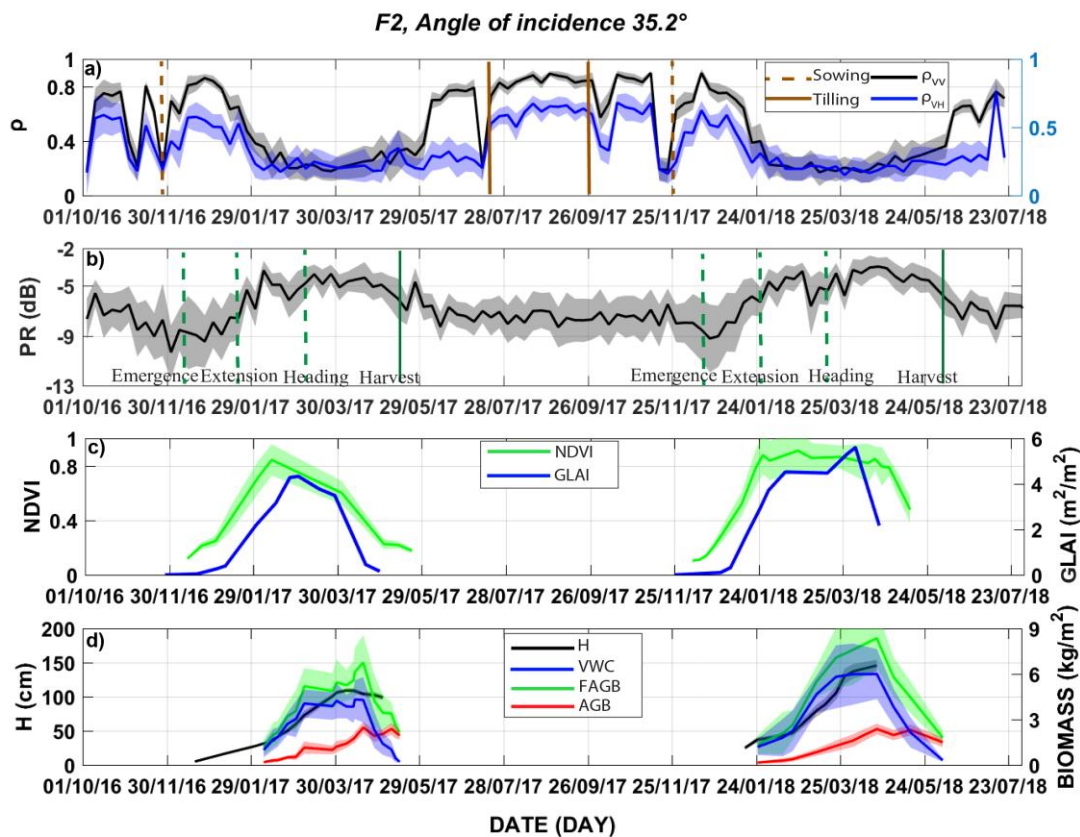**Figure A5. Time series of the backscattering coefficient at VV (a) and VH (b) polarizations on F2 at 35.2° of incidence angle during the period from October 01, 2016 to July 31, 2018. The tilling works and phenological stages of wheat are superimposed on subplots (a) and (b), respectively. The air temperature, Surface soil moisture (SSM), irrigation and rainfall are displayed on subplot (c).**
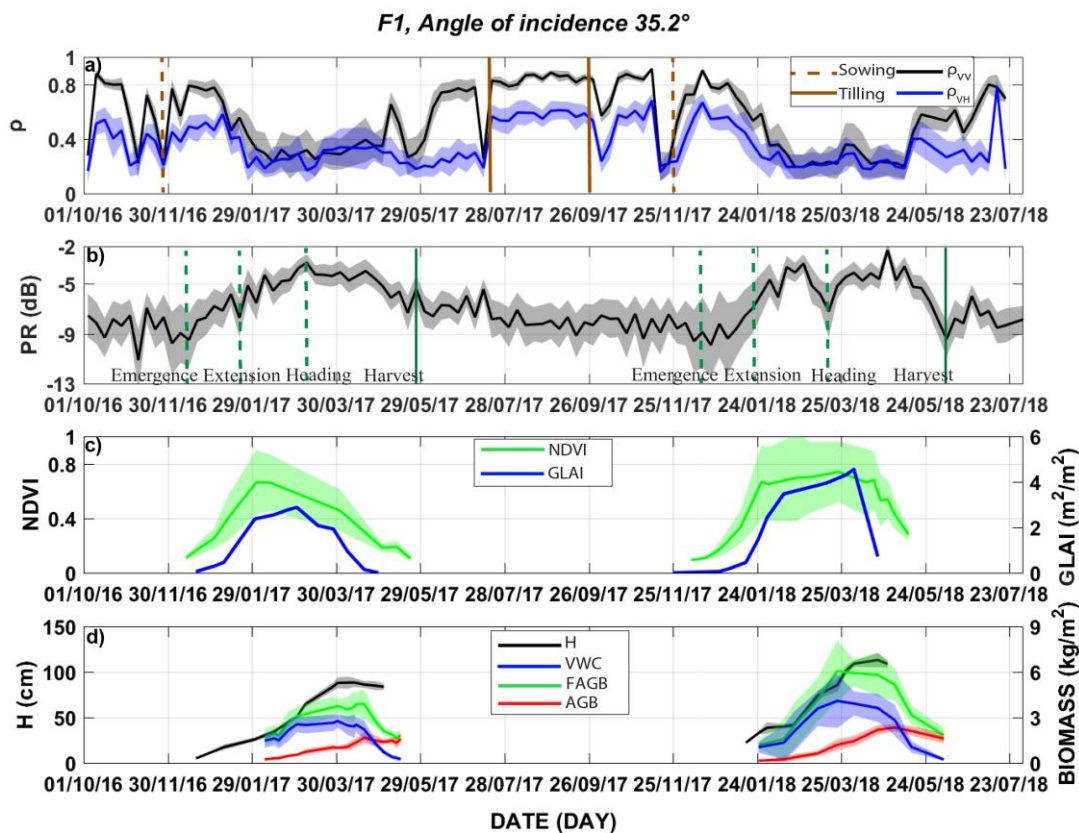
**Figure A6.** Time series of the interferometric coherence at VV and VH polarizations (a) and the polarization ratio (b) on F1 at 35.2° of incidence angle during the period from October 01, 2016 to July 31, 2018. The tilling works and phenological stages of wheat are superimposed on subplots (a) and (b), respectively. NDVI and measured GLAI are displayed in subplot (c). Measured H, FAGB, VWC and AGB are plotted in subplot (c). Time series are presented by mean values (solid lines) and standard deviations (filled fields surrounding the solid lines).

Figure A7. Time series of the interferometric coherence at VV and VH polarizations (a) and the polarization ratio (b) on F1 at 45.6° of incidence angle during the period from October 01, 2016 to July 31, 2018. The tilling works and pheneological stages of wheat are superimposed on subplots (a) and (b), respectively. NDVI and measured GLAI are displayed in subplot (c). Measured H, FAGB, VWC and AGB are plotted in subplot (c). Time series are presented by mean values (solid lines) and standard deviations (filled fields surrounding the solid lines).

Figure A8. Time series of the interferometric coherence at VV and VH polarizations (a) and the polarization ratio (b) on F2 at 35.2° of incidence angle during the period from October 01, 2016 to July 31, 2018. The tilling works and phenological stages of wheat are superimposed on subplots (a) and (b), respectively. NDVI and measured GLAI are displayed in subplot (c). Measured H, FAGB, VWC and AGB are plotted in subplot (c). Time series are presented by mean values (solid lines) and standard deviations (filled fields surrounding the solid lines).
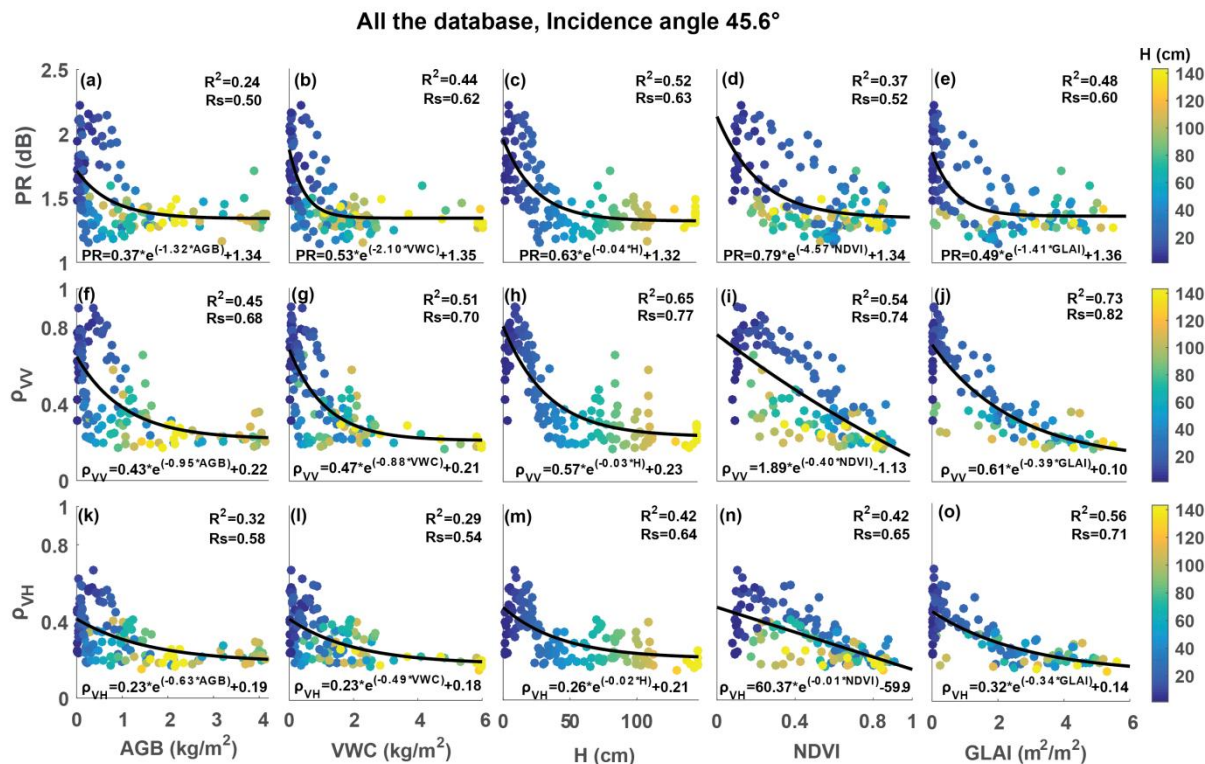
Figure A9. Scatterplots of the relationships between PR, ρ_{VV} and ρ_{VH} and AGB, VWC, H, NDVI and GLAI at 45.6° angle of incidence. The entire database is used from the three fields (F1, F2 and F3). H is used to monitor the evolution during the growing season. All the determination coefficient R^2 and the Spearman rank correlation Rs are significant at 99%.

Earth System
Science
Data

Open Access

Discussions

534 **Author contribution.** NO, LJ, JE and SK designed the experiments. NO, MK, JE, AC and AB carried the experiements out.

535 NO processed the Sentinel-1 products. NO, LJ, JE and SK analyzed the data. NO wrote the original draft and all the co-

536 authors contribute in the review and editing of the manuscript.

537 **Competing interests.** The authors declare that they have no conflict of interest.

Earth System
Science
Data
Discussions
Open Access

References

544

545 Abourida, A., Simonneaux, V., Errouane, S., Sighir, F., Berjami, B. and Sgir, F.: Estimation des volumes d'eau pompés dans la nappe pour
546 l'irrigation (Plaine du Haouz, Marrakech, Maroc). Comparaison d'une méthode statistique et d'une méthode basée sur l'utilisation de
547 données de télédétection, J. Water Sci., 21(4), 489–501 [online] Available from: https://hal.ird.fr/ird-00389822, 2008.

548 Allen, R. G., Pereira, L. S., RAES, D. and SMITH, M.: Crop Evapotranspiration—Guidelines for Computing Crop Water Requirements,
549 Irrigation and Drain, Paper No. 56. FAO, Rome, Italy,. [online] Available from: http://academic.uprm.edu/abe/backup2/tomas/fao 56.pdf,
550 1998.

551 Allmaras, R. R., Burwell, R. E., Larson, W. E. and Holt, R. F.: TOTAL POROSITY AND RANDOM ROUGHNESS OF THE
552 INTERROW ZONE AS INFLUENCED BY TILLAGE, USA. [online] Available from:
553 https://www.ars.usda.gov/ARSUserFiles/50701000/cswq-t1914-allmaras.pdf (Accessed 21 February 2020), 1966.

554 Bai, X., He, B., Li, X., Zeng, J., Wang, X., Wang, Z., Zeng, Y. and Su, Z.: First assessment of Sentinel-1A data for surface soil moisture
555 estimations using a coupled water cloud model and advanced integral equation model over the Tibetan Plateau, Remote Sens., 9(7), 1–20,
556 doi:10.3390/rs9070714, 2017.

557 Bamler, R. and Hartl, P.: Synthetic aperture radar interferometry, Inverse Probl., 14(4), 1–54, doi:10.1088/0266-5611/14/4/001, 1998.

558 Bigeard, G., Coudert, B., Chirouze, J., Er-Raki, S., Boulet, G. and Jarlan, L.: Estimating evapotranspiration with thermal infrared data over
559 Agricultural landscapes: comparison of a simple energy budget model and a svat model, in Estimation spatialisée de l'évapotranspiration à
560 l'aide de données infra-rouge thermique multi-résolutions, pp. 149–192, Toulouse., 2017.

561 Blaes, X. and Defourny, P.: Retrieving crop parameters based on tandem ERS 1 / 2 interferometric coherence images, Remote Sens.
562 Environ., 88(4), 374–385, doi:10.1016/j.rse.2003.08.008, 2003.

563 Brown, S. C. M., Quegan, S., Morrison, K., Bennett, J. C. and Cookmartin, G.: High-resolution measurements of scattering in wheat
564 canopies - Implications for crop parameter retrieval, IEEE Trans. Geosci. Remote Sens., 41(7 PART I), 1602–1610,
565 doi:10.1109/TGRS.2003.814132, 2003.

566 Castelli, M., Anderson, M. C., Yang, Y., Wohlfahrt, G., Bertoldi, G., Niedrist, G., Hammerle, A., Zhao, P., Zebisch, M. and Notarnicola,
567 C.: Two-source energy balance modeling of evapotranspiration in Alpine grasslands, Remote Sens. Environ., 209(February), 327–342,
568 doi:10.1016/j.rse.2018.02.062, 2018.

569 Chauhan, S., Shanker, H. and Patel, P.: Wheat crop biophysical parameters retrieval using hybrid-polarized RISAT-1 SAR data, Remote
570 Sens. Environ., 216, 28–43, doi:10.1016/j.rse.2018.06.014, 2018.

571 Cho, E., Choi, M. and Wagner, W.: An assessment of remotely sensed surface and root zone soil moisture through active and passive
572 sensors in northeast Asia, Remote Sens. Environ., 160, 166–179, doi:10.1016/j.rse.2015.01.013, 2015.

573 CNES: The ORFEO Tool Box Software Guide. [online] Available from: https://www.orfeo-toolbox.org/packages/OTBSoftwareGuide.pdf,
574 2018.

575 Das, N. N., Mohanty, B. P., Cosh, M. H. and Jackson, T. J.: Modeling and assimilation of root zone soil moisture using remote sensing
576 observations in Walnut Gulch Watershed during SMEX04, Remote Sens. Environ., 112, 415–429, doi:10.1016/j.rse.2006.10.027, 2008.

577 Ducrot, R., Page, C. Le, Bommel, P. and Kuper, M.: Articulating land and water dynamics with urbanization : an attempt to model natural
578 resources management at the urban edge, Comput. Environ. Urban Syst., 28, 85–106, 2004.

579 Dumedah, G., Walker, J. P. and Merlin, O.: Root-zone soil moisture estimation from assimilation of downscaled Soil Moisture and Ocean
580 Salinity data, Adv. Water Resour., 84, 14–22, doi:10.1016/j.advwatres.2015.07.021, 2015.

581 Van Emmerik, T., Steele-Dunne, S. C., Judge, J. and Van De Giesen, N.: Impact of Diurnal Variation in Vegetation Water Content on
582 Radar Backscatter from Maize During Water Stress, IEEE Trans. Geosci. Remote Sens., 53(7), 3855–3869,
583 doi:10.1109/TGRS.2014.2386142, 2015.

584 Engdahl, M. E., Borgeaud, M., Member, S. and Rast, M.: The Use of ERS-1 / 2 Tandem Interferometric Coherence in the Estimation of
585 Agricultural Crop Heights, IEEE Trans. Geosci. Remote Sens., 39(8), 1799–1806, doi:0.1109/36.942558, 2001.

586 Ezzahar, J., Ouaadi, N., Zribi, M., Elfarkh, J., Aouade, G., Khabba, S., Er-Raki, S., Chehbouni, A. and Jarlan, L.: Evaluation of
587 Backscattering Models and Support Vector Machine for the Retrieval of Bare Soil Moisture from Sentinel-1 Data, Remote Sens., 12(1),
588 72, doi:10.3390/rs12010072, 2020.

589 Fader, M., Shi, S., Bondeau, A. and Cramer, W.: Mediterranean irrigation under climate change : more efficient irrigation needed to
590 compensate for increases in irrigation water requirements, Hydrol. Earth Syst. Sci., 20, 953–973, doi:10.5194/hess-20-953-2016, 2016.

591 Farineau, J. and Morot-Gaudry, J.-F.: La photosynthèse: Processus physiques, moléculaires et physiologiques, Quae., Paris. [online]
592 Available from: https://books.google.fr/books?id=UHBJDwAAQBAJ (Accessed 30 August 2020), 2018.

593 Fieuzal, R., Baup, F. and Marais-Sicre, C.: Monitoring Wheat and Rapeseed by Using Synchronous Optical and Radar Satellite Data—
594 From Temporal Signatures to Crop Parameters Estimation, Adv. Remote Sens., 02(02), 162–180, doi:10.4236/ars.2013.22020, 2013.

595 Fontanelli, G., Paloscia, S., Pampaloni, P., Pettinato, S., Santi, E., Montomoli, F., Brogioni, M. and Macelloni, G.: HydroCosmo: The
596 monitoring of hydrological parameters on agricultural areas by using Cosmo-SkyMed images, Eur. J. Remote Sens., 46(1), 875–889,
597 doi:10.5721/EuJRS20134652, 2013.

598 Ford, T. W., Harris, E. and Quiring, S. M.: Estimating root zone soil moisture using near-surface observations from SMOS, Hydrol. Sci. J.,
599 18, 139–154, doi:10.5194/hess-18-139-2014, 2014.

600 Gherboudj, I., Magagi, R., Berg, A. A. and Toth, B.: Soil moisture retrieval over agricultural fields from multi-polarized and multi-angular
601 RADARSAT-2 SAR data, Remote Sens. Environ., 115(1), 33–43, doi:10.1016/j.rse.2010.07.011, 2011.

602 Giorgi, F.: Climate change hot-spots, Geophys. Res. Lett., 33(8), 1–4, doi:10.1029/2006GL025734, 2006.

603 Giorgi, F. and Lionello, P.: Climate change projections for the Mediterranean region, Glob. Planet. Change, 63, 90–104,
604 doi:10.1016/j.gloplacha.2007.09.005, 2008.

605 Girard, M. C. (Michel C. and Girard, C. M. (Colette M.: Télédétection appliquée : zones tempérées et intertropicales , Paris., edited by
606 MASSON., 1989.

607 Gorrab, A., Zribi, M., Baghdadi, N., Mougenot, B., Fanise, P. and Chabaane, Z. L.: Retrieval of both soil moisture and texture using
608 TerraSAR-X images, Remote Sens., 7(8), 10098–10116, doi:10.3390/rs70810098, 2015.

609 Hagolle, O., Huc, M., Pascual, D. V. and Dedieu, G.: A multi-temporal and multi-spectral method to estimate aerosol optical thickness
610 over land, for the atmospheric correction of FormoSat-2, LandSat, VENμS and Sentinel-2 images, Remote Sens., 7(3), 2668–2691,
611 doi:10.3390/rs70302668, 2015.

612 El Hajj, M., Baghdadi, N., Zribi, M., Belaud, G., Cheviron, B., Courault, D. and Charron, F.: Soil moisture retrieval over irrigated
613 grassland using X-band SAR data, Remote Sens. Environ., 176, 202–218, doi:10.1016/j.rse.2016.01.027, 2016.

614 El Hajj, M., Baghdadi, N., Bazzi, H. and Zribi, M.: Penetration Analysis of SAR Signals in the C and L Bands for Wheat, Maize, and
615 Grasslands, Remote Sens., 11(1), 22–24, doi:10.3390/rs11010031, 2019.

616 Holah, N., Baghdadi, N., Zribi, M., Bruand, A. and King, C.: Potential of ASAR/ENVISAT for the characterization of soil surface
617 parameters over bare agricultural fields, Remote Sens. Environ., 96(1), 78–86, doi:10.1016/j.rse.2005.01.008, 2005.

618 Hosseini, M. and McNairn, H.: Using multi-polarization C- and L-band synthetic aperture radar to estimate biomass and soil moisture of
619 wheat fields, Int. J. Appl. Earth Obs. Geoinf., 58, 50–64, doi:10.1016/j.jag.2017.01.006, 2017.

620 IPCC: Climate Change 2014: Synthesis Report. Contribution of Working Groups I, II and III to the Fifth Assessment Report of the
621 Intergovernmental Panel on Climate Change [Core Writing Team, R.K. Pachauri and L.A. Meyer (eds.)], Geneva, Switzerland., 2014.

622 Jarlan, L., Khabba, S., Er-Raki, S., Le Page, M., Hanich, L., Fakir, Y., Merlin, O., Mangiarotti, S., Gascoin, S., Ezzahar, J., Kharrou, M.
623 H., Berjamy, B., Saaïdi, A., Boudhar, A., Benkaddour, A., Laftouhi, N., Abaoui, J., Tavernier, A., Boulet, G., Simonneaux, V., Driouech,
624 F., El Adnani, M., El Fazziki, A., Amenzou, N., Raibi, F., El Mandour, H., Ibouh, H., Le Dantec, V., Habets, F., Tramblay, Y., Mougenot,
625 B., Leblanc, M., El Faïz, M., Drapeau, L., Coudert, B., Hagolle, O., Filali, N., Belaqziz, S., Marchane, A., Szczypta, C., Toumi, J., Diarra,
626 A., Aouade, G., Hajhouji, Y., Nassah, H., Bigeard, G., Chirouze, J., Boukhari, K., Abourida, A., Richard, B., Fanise, P., Kasbani, M.,
627 Chakir, A., Zribi, M., Marah, H., Naimi, A., Mokssit, A., Kerr, Y. and Escadafal, R.: Remote Sensing of Water Resources in Semi- Arid
628 Mediterranean Areas : the joint international laboratory TREMA, Int. J. Remote Sens., 36(19–20), 4879–4917,
629 doi:10.1080/01431161.2015.1093198, 2015.

630 Jarlan, L., Khabba, S., Szczypta, C., Lili-Chabaane, Z., Driouech, F., Le Page, M., Hanich, L., Fakir, Y., Boone, A. and Boulet, G.: Water
631 resources in South Mediterranean catchments Assessing climatic drivers and impacts Water resources, in The Mediterranean Region
632 under Climate Change, Marseille., 2016.

633 Lee, C., Lu, Z. and Jung, H.: Simulation of time-series surface deformation to validate a multi- interferogram InSAR processing technique,
634 Int. J. Remote Sens., 33(22), 7075–7087, doi:10.1080/01431161.2012.700137, 2012.

635 Li, J. and Wang, S.: Using SAR-derived vegetation descriptors in a water cloud model to improve soil moisture retrieval, Remote Sens.,
636 10(9), doi:10.3390/rs10091370, 2018.

637 Li, Y. Y., Zhao, K., Ren, J. H., Ding, Y. L. and Wu, L. L.: Analysis of the dielectric constant of saline-alkali soils and the effect on radar
638 backscattering coefficient: A case study of soda alkaline saline soils in western Jilin province using RADARSAT-2 data, Sci. World J., 1–
639 14, doi:10.1155/2014/563015, 2014.

640 Major, D. G., Schaalje, G. B., Asrar, G. and Kanemasu, E. T.: ESTIMATION OF WHOLE-PLANT BIOMASS AND GRAIN YIELD
641 FROM SPECTRAL REFLECTANCE OF CEREALS, Can. J. Remote Sens., 12(I), 47–54, 1986.

642 Mattia, F., Le Toan, T., Picard, G., Posa, F. I., D'Alessio, A., Notarnicola, C., Gatti, A. M., Rinaldi, M., Satalino, G. and Pasquariello, G.:
643 Multitemporal C-band radar measurements on wheat fields, IEEE Trans. Geosci. Remote Sens., 41(7 PART I), 1551–1560,
644 doi:10.1109/TGRS.2003.813531, 2003.

645 Ministre de l'agriculture et peche maritime du develpement rurale et des eaux et forets, Ed.: Agriculture en chiffres 2017, 2018th ed.,
646 PLAN MAROC VERT. [online] Available from: http://www.agriculture.gov.ma/sites/default/files/AgricultureEnChiffre2017VAVF.pdf,
647 2018.

648 Mission, R. O. and Services, G. O.: ESA's Radar Observatory Mission for GMES Operational Services, SP-1322/1., 2012.

649 Morrison, K., Bennett, J. C., Nolan, M. and Menon, R.: Laboratory Measurement of the DInSAR Response to Spatiotemporal Variations
650 in Soil Moisture - IEEE Journals & Magazine, IEEE Trans. Geosci. Remote Sens., 49(10), 3815–3823, doi:10.1109/TGRS.2011.2132137,
651 2011.

652 Nolin, M. ., Quenum, M., Cambouris, A. ., Martin, A. and Cluis, D.: Rugosité de la surface du sol – description et interprétation, Agrosol,
653 16(1), 5–21, 2005.

654 Norman, J. M., Kustas, W. P. and Humes, K. S.: Source approach for estimating soil and vegetation energy fluxes in observations of
655 directional radiometric surface temperature, Agric. For. Meteorol., 77(3–4), 263–293, doi:10.1016/0168-1923(95)02265-Y, 1995.

656 Ouaadi, N., Ezzahar, J., Khabba, S., Er-Raki, S., Chakir, A., Ait Hssaine, B., Le Dantec, V., Rafi, Z., Beaumont, Antoine; Kasbani, M. and
657 Jarlan, L.: C-band radar data and in situ measurements for the monitoring of wheat crops in a semi-arid area (center of Morocco),
658 DataSuds, [online] Available from: https://doi.org/10.23708/8D6WQC, 2020a.

659 Ouaadi, N., Jarlan, L., Ezzahar, J., Zribi, M., Khabba, S., Bouras, E., Bousbih, S. and Frison, P.: Monitoring of wheat crops using the
660 backscattering coe ffi cient and the interferometric coherence derived from Sentinel-1 in semi-arid areas, Remote Sens. Environ., 251(C),
661 doi:10.1016/j.rse.2020.112050, 2020b.

662 Ouaadi, N., Jarlan, L., Ezzahar, J., Zribi, M., Khabba, S., Bouras, E. and Frison, P.-L.: Surface Soil Moisture Retrieval Over Irrigated
663 Wheat Crops in Semi-Arid Areas using Sentinel-1 Data, in 2020 IEEE Mediterranean and Middle-East Geoscience and Remote Sensing
664 Symposium (M2GARSS), pp. 212–215., 2020c.

665 Ouaadi, N., Jarlan, L., Ezzahar, J., Khabba, S., Dantec, V. Le, Rafi, Z., Zribi, M. and Frison, P.-L.: Water Stress Detection Over Irrigated
666 Wheat Crops in Semi-Arid Areas using the Diurnal Differences of Sentinel-1 Backscatter, in 2020 IEEE Mediterranean and Middle-East
667 Geoscience and Remote Sensing Symposium (M2GARSS), pp. 306–309., 2020d.

668 Patel, P., Srivastava, H. S. and Navalgund, R. R.: Estimating wheat yield: an approach for estimating number of grains using cross-
669 polarised ENVISAT-1 ASAR data, Microw. Remote Sens. Atmos. Environ. V, 6410, 641009, doi:10.1117/12.693930, 2006.

670 Periasamy, S.: Significance of dual polarimetric synthetic aperture radar in biomass retrieval : An attempt on Sentinel-1, Remote Sens.
671 Environ., 217, 537–549, doi:10.1016/j.rse.2018.09.003, 2018.

672 Petcu, E., Petcu, G., Lazãr, C. and Vintilã, R.: Relationship between leaf area index, biomass and winter wheat yield obtained at fundulea,
673 under conditions of 2001 year, Rom. Agric. Res., 19–20, 21–29, 2003.

674 Picard, G., Toan, T. Le and Mattia, F.: Understanding C-Band Radar Backscatter From Wheat Canopy Using a Multiple-Scattering
675 Coherent Model, IEEE Trans. Geosci. Remote Sens., 41(7), 1583–1591, doi:10.1109/TGRS.2003.813353, 2003.

676 Rodell, M., Houser, P. R., Jambor, U., Gottschalck, J., Mitchell, K., Memg, C.-J., Arsenault, K., Cosgrove, B., Radakovich, J., Bosilovich,
677 M., Entin, J. K., Walker, J. P., Lohmann, D. and Toll, D.: THE GLOBAL LAND DATA ASSIMILATION SYSTEM, Bull. Am. Meteorol.
678 Soc., 85(3), 381–394, doi:10.1175/BAMS-85-3-381, 2004.

679 Sabater, J. M., Jarlan, L., Calvet, J.-C. and Bouyssel, F.: From Near-Surface to Root-Zone Soil Moisture Using Different, J. Hydrol., 8,

680   194–206, doi:10.1175/JHM571.1, 2006.

681   Scott, C. P., Lohman, R. B. and Jordan, T. E.: InSAR constraints on soil moisture evolution after the March 2015 extreme precipitation
682   event in Chile, Sci. Rep., 7(1), doi:10.1038/s41598-017-05123-4, 2017.

683   Small, D. and Schubert, A.: Guide to ASAR Geocoding, ESA-ESRIN Tech. Note RSL-ASAR-GC-AD, (1.01), 1–36, doi:RSL-ASAR-GC-
684   AD, 2008.

685   Sure, A. and Dikshit, O.: Estimation of root zone soil moisture using passive microwave remote sensing : A case study for rice and wheat
686   crops for three states in the Indo- Gangetic basin, J. Environ. Manage., 234, 75–89, doi:10.1016/j.jenvman.2018.12.109, 2019.

687   Taconet, O., Benallegue, M., Vidal-Madjar, D., Prevot, L., Dechambre, M. and Normand, M.: Estimation of soil and crop parameters for
688   wheat from airborne radar backscattering data in C and X bands, Remote Sens. Environ., 50(3), 287–294, doi:10.1016/0034-
689   4257(94)90078-7, 1994.

690   Torres, R., Snoeij, P., Geudtner, D., Bibby, D., Davidson, M., Attema, E., Potin, P., Rommen, B., Floury, N., Brown, M., Navas, I.,
691   Deghaye, P., Duesmann, B., Rosich, B., Miranda, N., Bruno, C., Abbate, M. L., Croci, R., Pietropaolo, A., Huchler, M. and Rostan, F.:
692   GMES Sentinel-1 mission, Remote Sens. Environ., 120, 9–24, doi:10.1016/j.rse.2011.05.028, 2012.

693   Touzi, R., Lopes, A., Bruniquel, J. and Vachon, P. W.: Coherence estimation for SAR imagery, IEEE Trans. Geosci. Remote Sens., 37(1
694   PART 1), 135–149, doi:10.1109/36.739146, 1999.

695   Ulaby, F., Moore, R. and Fung, A.: Microwave remote sensing active and passive-volume III: from theory to applications. [online]
696   Available from: https://infoscience.epfl.ch/record/51983 (Accessed 10 August 2018), 1986.

697   Ulaby, F. T. and Batlivala, percy P.: Optimum Radar Parameters for Mapping Soil Moisture, IEEE Trans. Geosci. Electron., GE-14(2),
698   81–93, 1976.

699   Ulaby, F. T. and Dobson, M. C.: Microwave Soil Moisture Research, IEEE Trans. Geosci. Remote Sens., GE-24(1), 23–36,
700   doi:10.1109/TGRS.1986.289585, 1986.

701   Ulaby, F. T., Aslam, A. and Dobson, M. C.: Effects of Vegetation Cover on the Radar Sensitivity to Soil Moisture, IEEE Trans. Geosci.
702   Remote Sens., GE-20(4), 476–481, doi:10.1109/TGRS.1982.350413, 1982.

703   Veloso, A., Mermoz, S., Bouvet, A., Le Toan, T., Planells, M., Dejoux, J. F. and Ceschia, E.: Understanding the temporal behavior of
704   crops using Sentinel-1 and Sentinel-2-like data for agricultural applications, Remote Sens. Environ., 199, 415–426,
705   doi:10.1016/j.rse.2017.07.015, 2017.

706   Wang, H., Magagi, R. and Goïta, K.: Potential of a two-component polarimetric decomposition at C-band for soil moisture retrieval over
707   agricultural fields, Remote Sens. Environ., 217, 38–51, doi:10.1016/j.rse.2018.08.003, 2018.

708   Wang, P., Song, X., Han, D., Zhang, Y. and Zhang, B.: Determination of evaporation , transpiration and deep percolation of summer corn
709   and winter wheat after irrigation, Agric. Water Manag., 105, 32–37, doi:10.1016/j.agwat.2011.12.024, 2012.

710   Wegmuller, U. and Werner, C.: Retrieval of Vegetation Parameters with SAR Interferometry, IEEE Trans. Geosci. Remote Sens., 35(1),
711   18–24, doi:10.1109/36.551930, 1997.

712   Zan, F. De and Guarnieri, A. M.: TOPSAR : Terrain Observation by Progressive Scans, IEEE Trans. Geosci. Remote Sens., 44(9), 2352–
713   2360, doi:10.1109/TGRS.2006.873853, 2006.

714   De Zan, F., Parizzi, A., Prats-Iraola, P. and López-dekker, P.: A SAR Interferometric Model for Soil Moisture, IEEE Trans. Geosci.
715   Remote Sens., 52(1), 418–425, 2014.

716   Zribi, M., Kotti, F., Amri, R., Wagner, W., Shabou, M., Lili-Chabaane, Z. and Baghdadi, N.: Soil moisture mapping in a semiarid region,
717   based on ASAR/Wide Swath satellite data, Water Resour. Res., doi:10.1002/2012WR013405, 2014.

718